

## An ML-based framework for predicting prestressing force reduction in reinforced concrete box-girder bridges with unbonded tendons

Mirko Calò<sup>a</sup>, Sergio Ruggieri<sup>a,\*</sup>, Manuel Buitrago<sup>b</sup>, Andrea Nettis<sup>a</sup>, Jose M. Adam<sup>b</sup>, Giuseppina Uva<sup>a</sup>

<sup>a</sup> DICATECH Department, Polytechnic University of Bari, via E. Orabona 4, 70125 Bari, Italy

<sup>b</sup> ICITECH, Universitat Politècnica de València, Camino de Vera s/n, 46022 Valencia, Spain

### ARTICLE INFO

**Keywords:**  
 Existing bridges  
 Bridge assessment  
 Structural monitoring  
 Box-girder bridges  
 Machine learning  
 Prestressing force

### ABSTRACT

The paper presents a machine learning (ML) based framework to predict the prestressing force reduction in prestressed reinforced concrete (PSC) box-girder bridges with unbonded tendons. In the field of road network safety, the reliable assessment of some bridge typologies, such as PSC box-girder bridges, depends on different aspects, among which the inaccessibility of internal unbonded tendons, the difficulty in measuring the effective prestressing force reduction over time, the design of an efficient structural health monitoring (SHM) system. To address the above issues, the proposed approach exploits the results of experimental tests on a scaled PSC box-girder to validate a nonlinear modelling strategy and, in turn, to generate a sample dataset for training different ML algorithms. To ensure generalizability of the proposed ML model, the variability of several parameters, including geometrical and mechanical properties, was accounted for. The obtained results, evaluated in terms of statistical metrics and through an eXplainability approach, revealed that the proposed surrogate model is able to predict the prestressing force reduction for this bridge typology, knowing the current prestressing force, the elastic modulus of the concrete, and the strain variation in specific cross-sections of the structure. The application of the framework on a scaled PSC box-girder experimentally tested, demonstrated its suitability for: i) estimating the prestressing force reduction without employing periodic and expensive onsite tests; and ii) providing the best strategy for employing a sensor-based SHM system.

### 1. Introduction

The safety of existing bridges is a primary concern for road and railway management companies and public institutions, which through a wide range of activities continuously assess the health state of bridge portfolios to reduce the risk for safeguarding human life and minimizing economic losses. When referring to bridge portfolios, the main challenge is to individuate the assets characterized by poor structural conditions and, subsequently, to perform structure-specific analysis (e.g., structural health monitoring - SHM, onsite inspection campaign or detailed assessment via modelling and analysis) to plan future actions, such as demolition/reconstruction, retrofit interventions or traffic limitations. This is the logic behind current trends in risk-prioritization strategies of existing bridge portfolios, such as the one proposed by the Italian government that, after the collapses of some important bridges (i.e., [1,2]), released new guidelines for the structural safety of existing bridges and viaducts [3]. Risk-informed prioritization through a large-scale

screening of bridge portfolios is fundamental in driving the few available resources towards bridges with higher risks, as highlighted by Adam et al. [4]. Overall, the above approach was designed to be applied on the entire national bridge stock, which is characterized by different typologies of bridges, such as prestressed reinforced concrete (PSC) ones. Taking as reference the Italian case, according to the onsite inspections performed by the Fabre Consortium [5], over a sample of 400 bridges, around 67 % are represented by PSC bridges. The superstructure of this bridge typology is not only designed with T or double-T beams, but other shapes exist, such as the box-girder ones. In Italy, PSC box-girder bridges were conceived and built from the second half of 50's onwards, presenting some peculiarities and main advantages, such as a high torsional stiffness (especially for curved bridges and for high eccentric loads), and the possibility to reduce the deck height while ensuring long spans. In addition, the use of prestressing technology (usually through the post-tension approach) allowed mitigating the effect of bending moment induced by external loads and the tensile stress

\* Corresponding author.

E-mail address: [sergio.ruggieri@poliba.it](mailto:sergio.ruggieri@poliba.it) (S. Ruggieri).

in reinforced concrete (RC) sections and increasing the robustness of the structure through hyperstatic schemes [6].

Nevertheless, different issues characterize the assessment of this bridge typology. The first issue regards the onsite inspection of the box-girder, in which the external surface can be directly surveyed as for other PSC bridges, while special inspections are required inside the box. This area is characterized by specific problems, such as defects on the internal concrete surface, corrosion on the steel tendons, presence of water deriving from malfunctioning longitudinal joints (if present) [7]. Still, special inspections are not always possible, unless manholes are planned during the design phase [8]. The second issue consists of assessing the prestressing force and the related reduction over time. Several studies investigated this problem (e.g., [9–12]), showing objective difficulties in assessing its effective value on existing bridges, due to time-dependent phenomena, environmental parameters, and the interaction among degradation processes [13]. As pointed out by Huang et al. [14] and reported in building codes (e.g., [15,16]), both concrete and harmonic steel used in PSC structures are affected by long-term deformations. Concrete is subjected to volume changes due to shrinkage and creep, with different time rates. Shrinkage is influenced by concrete curing conditions and affects the elastic modulus of concrete, while creep is dependent on the stress level of the section and the bridge configuration during construction phases. Strain increments induced by creep phenomenon must be considered for each different cross-section of the box-girder where geometrical characteristics of the beam changes along its longitudinal development (e.g., the number of tendons and section depth). On the other side, long-term relaxation of prestressing tendons, when axially deformed by a tensile force [17], must be addressed through proper analysis, involving constitutive material laws (e.g., viscoplastic constitutive relation proposed by Bažant and Yu [18]), environmental factors, and construction quality of the prestressing process (e.g., partial grouting [19,20]). All the above phenomena reduce the initial prestressing force applied to the tendons, and this reduction is estimated around 20 % during an average period of 50 years after the end of the bridge construction, as reported in [21]. Phenomena characterizing the service life of bridges, such as corrosion can still reduce both the mechanical properties (i.e., ultimate strength and ultimate strain) and the cross-sectional area and mass of the steel strands [22], leading in worst cases to wires rupture, which reduces the total prestressing force of tendons at the anchorage and thus the bearing capacity of structural elements [23,24].

A viable option to monitor the prestressing force reduction over time could be the design and predisposition of a specific SHM system (e.g., [25,26]), able to reveal the variation of the force level and simulate the current service life of PSC bridges in a model updating process [14]. Regarding PSC box-girder, a third issue is the difficulty of setting up an effective SHM system, for different technical reasons. Depending on the physical, chemical, and dynamic parameters of interest, specific sensors are required, and their number and position must be evaluated case-by-case [27]. In addition, a large amount of data should be stored and processed to ensure quasi-real-time monitoring [28]. Over time, several SHM approaches were proposed by scientific literature. Starting from the most traditional approaches, Sousa et al. [29] employed sensors to monitor deterioration mechanisms over time of the Lezíria Bridge. After providing some general rules for designing the monitoring system, the authors evaluated the serviceability, the reliability of the structure, and the remaining service life of the bridge in terms of durability, also accounting for the prestressing force level. Dall'Asta and Lenzi [30] analysed a class of PSC beams characterized by unbonded internal strands via vibration method. Frequencies of the first vertical and horizontal bending vibration modes were slightly modified by the variations of stress and profile of the strands, while a stronger influence was observed for the first twisting vibration mode. Similar outcomes were obtained in other studies ([31–35]) showing that vibration methods were not effective in detecting prestressing losses, especially if other effects were not considered (e.g. concrete cracking, material

degradation, and variation of environmental conditions). Another monitoring approach to detect prestressing force reduction was represented by impedance-based methods, in which load cells like piezoelectric sensors are used to monitor the variation of prestressing force through the electrical charge produced by mechanically stressing the tendons or the region where they are applied [36]. Although impedance-based methods showed good potentialities (e.g., [37,38]), several limitations were identified, such as the strong sensitivity of the adopted device to temperature and difficulties in reaching tendon anchorages for sensor application. Modern approaches are represented by the strain-based method, which allows long-term monitoring of both concrete and tendon strain. Different types of strain sensors can be used, such as in-strand fiber Bragg gratings (FBG) sensors [39–41] and concrete strain sensors [42,43]. Nevertheless, there are some limitations for existing bridges. In fact, in-strand FBG sensors can be effective only if equipped in the construction phase. On the other hand, concrete strain sensors can be placed in each desired section and in variable number (e.g., bottom and top part of the section). These are more effective in the case of linear strain distribution and a perfect bond between the prestressing strands and surrounding concrete [44]. In the case of unbonded strands, as occurs for PSC box-girder bridges, it is not possible to establish a direct correlation between the strain of strands and of concrete fibers around the strand. Another promising investigation method proposed by Bonopera and Chang [45] is based on static deflections under three-point bending test. Following the vertical load application, the method estimates the prestressing force by measuring the vertical deflection at a quarter or at the midspan of the PSC girder-bridge. Interested readers can reference to [46] for a deeper discussion about methods used in the assessment of prestressing force and the related reduction over time.

In the last years, with the advent of new technologies, Machine Learning (ML) algorithms represented a consistent support to all phases of existing bridge health management, such as visual inspections (e.g., [47,48]), SHM (e.g., [49–51]) and risk assessment (e.g., [52–56]). Scientific literature proposes some applications regarding the combination of ML algorithms to SHM data for PSC girder bridge assessment. Dang et al. [57] presented a hybrid method relating Finite Element (FE) model and Artificial Neural Networks (ANNs) to evaluate strand relaxation in post-tensioned systems. ANNs were trained with numerical strain datasets obtained by FE model and the method was tested on a nine-strand anchorage, showing good potentialities for onsite implementation. Mariniello et al. [58] used a FE model for damage simulation and data extraction, aimed at training a specific ANN to detect tendon malfunctions in PSC bridges. The obtained results, compared with other ML algorithms like Random Forrest Regressor (RFR) and Support Vector Regression (SVR), showed the higher suitability of ANN model for the case studied. Kim and Park [59] proposed an ANN trained on experimental datasets to estimate the tensile stress on a 50-m real-scale PSC girder with embedded elasto-magnetic sensors. Results suggested the method could be a good solution for supporting SHM in on-field applications. Nguyen et al. [60] employed a Convolutional Neural Network to automatically extract optimal damage features from the raw impedance signals of piezoelectric sensors, demonstrating successful estimation of the prestressing loss in a PSC girder. This literature review about ML showed promising support in estimating the prestressing losses of unbonded tendons and in indicating the best practices to design sensors-based SHM systems. On this basis, this paper presents a new ML surrogate model, able to predict the prestressing force reduction in PSC box-girder bridges characterized by an unbonded post-tensioning system. In detail, the methodology described in Section 2 is designed to predict the variation of the prestressing force ( $F_1$ ), starting from its initial value ( $F_0$ ) and other mechanical features at the time of onsite strain-sensors installation (henceforth referred to as the time of the investigation, and herein indicated as “initial state”). Three of the most common supervised regression ML algorithms (i.e., ANN, RFR and SVR) are proposed as ML surrogate models of the structure. These algorithms

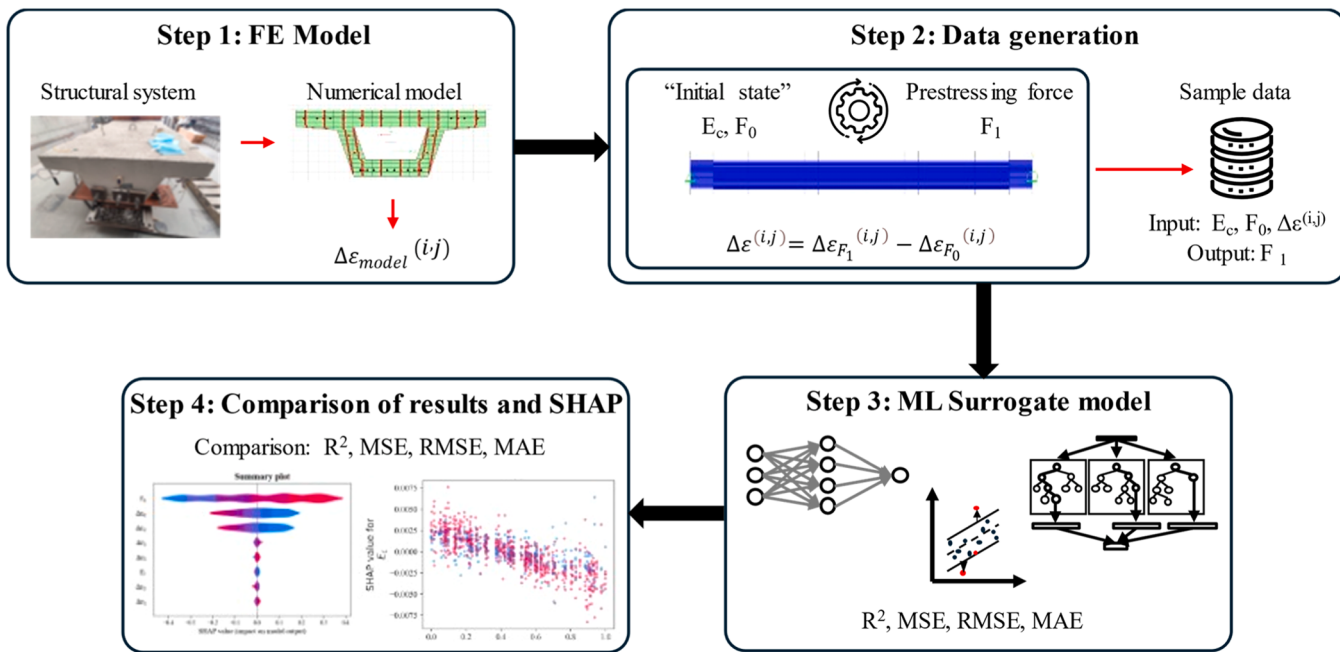


Fig. 1. Workflow of the proposed ML surrogate model.

were trained and tested over sample data generated with a nonlinear FE modelling approach, while the ML surrogate model was selected based on proper statistical metrics. To address the proper design of a sensors-based SHM system, the physical description of results is performed through an eXplainability approach, named SHapley Additive exPlanation (SHAP) [61] (see later for more details). The effectiveness of the framework and of the nonlinear FE modelling strategy was validated in Section 3 by the results derived by experimental tests on a scaled beam specimen made in the ICITECH laboratories of the *Universitat Politècnica de València*. ANN was identified as the best ML surrogate model for this application task and the most influent parameters on the prestressing force reduction were derived by the SHAP approach. From the obtained results, new insights were derived, which could be used in the design of an optimized sensor-based SHM for the most relevant structural parts. Finally, Section 4 draws the main conclusions of the study.

## 2. Proposed ML surrogate model

The proposed ML surrogate model is based on a model-driven approach, accounting for both physical and mathematical methods to establish the input-output relationship. The output of the model is the estimation of the current prestress level  $F_1$  value, given some input variables: the prestressing force ( $F_0$ ) and the elastic modulus of concrete ( $E_c$ ) at the time of onsite strain-sensors installation, and the values of strain variations ( $\Delta\epsilon^{(i,j)}$ ) for different fibers (indicated with the superscript  $(j)$ ) of different sections of the girder, (indicated with the superscript  $(i)$ ). It is worth specifying that input quantities are referred to at the time in which the deformation sensors are installed, and for this reason, the proposed model can predict the prestressing losses from that time onwards. The adopted model is not aimed at estimating prestressing losses occurred during the whole bridge lifetime, unless the bridge was not monitored and characterized from the end of the construction phase. The general framework of the proposed procedure is shown in Fig. 1, and all steps are detailed in the next Sections.

### 2.1. FE modelling strategy

The first step of the proposed framework consists of defining a

nonlinear FE model of the structure, given: (i) geometry of the PSC box-girder bridge (i.e., length of the spans, dimensions of the sections, position of the steel rebars and tendons in each section); (ii) information about prestressing force, i.e., the value of  $F_0$  and moment due to the eccentricity of  $F_0$  from the centroid of each section; (iii) mechanical properties of structural materials (i.e., concrete, harmonic and mild steel) and the related constitutive laws; (iv) boundary conditions (i.e., stiffness of supports). The choice of the type of numerical FE model represents a trade-off between accuracy and simplicity of the simulation. While accurate models, as the ones proposed by [62,63], ensure higher fidelity with the ground truth, simpler models are desired when modelling and analysing thousands of models, as occurs when dealing with sample data generation for training a ML model. If a detailed modelling strategy (e.g., micro-modelling through solid elements) was adopted it can also imply the characterization of other parameters not herein considered, such as the variation of the density of the concrete along the bridge development, or the effective stiffness of the supports. A good compromise ensuring both simplicity and accuracy of the FE model consists of using frame elements, characterized by correct boundary conditions (e.g., external restraints) accounting for both mechanical and geometrical nonlinearities. Given the different locations of unbonded tendons over the longitudinal development of the PSC box-girder bridge, a diffused plasticity approach is suggested, in which different sections are simulated through a fiber approach. In addition, this modelling approach dealing with the necessity to capture the evolution of strains in fibers located in different sections (i.e.,  $\Delta\epsilon^{(i,j)}$ ), is suitable for providing some insights about the design of effective SHM strategies. Obviously, the numerical model should record the strain values induced on the sections,  $i$ , and fibers  $j$ , subjected to sensor-based monitoring. It is worth noting that the numerical simulation of a prestressed beam could also be processed through a linear (or nonlinear) elastic model, considering the beneficial effects of the prestressing in reducing cracking and crushing phenomena. On the other hand, a nonlinear modelling approach was preferred, in this study, to account for low cracking and for extreme situations (e.g., low prestressing force values) in data generation and for geometric nonlinearities.

Regarding the typology of plasticity to implement in the FE model, a deformation-controlled PMM plasticity is suggested, which allows accounting for the presence of axial load due to prestressing (i.e.,  $P$ ) and

the bi-directional bending in both main section axis (i.e., MM). To model the prestressing loading induced by the unbonded post-tension system, an axial force can be applied in the centroid of the considered section together with proper bending moments attributed to the identified sections to simulate the position of the tendons [64] (i.e., external sections and intermediate ones considered in the diffused plasticity). From a mechanical point of view, the stress induced on each tendon by the prestressing force reduces yielding and ultimate stress of the steel material available for additional external loads (i.e., traffic loads). Thus, these mechanical properties are reduced by a quantity equal to the prestressing force times the cross area of the tendons. Concerning the mechanical nonlinearities, each fiber should be modelled in elastic and post-elastic fields, by assigning a proper constitutive law for each material typology. About this aspect, the selection of the constitutive laws depends on the analyst's preference and on the adopted software. As more practical options (and according to the authors' selection), the Mander model, as reported in the reference building code (Eurocode 2 [65]), can be used as concrete constitutive law for concrete fibers, while steel reinforcements can be simulated through a perfectly elastoplastic model.

According to the above-reported modelling strategy, some considerations can be provided. First, the definition of a nonlinear numerical model allows the reduction of the number of input parameters in the proposed ML model. Indeed, running several analyses under different prestressing load conditions (i.e.,  $F_0$ ) can provide the necessary output values to be used in the ML model (i.e.,  $\Delta\epsilon^{(i,j)}$ ), which accounts for the nonlinear nature of the investigated problem. Second, the proposed numerical model could be considered as simplified (e.g., simulation of the unbonded strands as external and punctual actions). If on one hand, this could represent a formal limitation of the proposed modelling strategy, on the other hand, this strongly lightens the computational time of analysis increasing the number of simulations for providing a consistent dataset for ML model training and test. For any cases, the quality of the model can be always assessed and validated towards experimental results (as done in the present study and as later shown). Finally, a clear simplification is hidden in the proposed model, because the physical variation of  $F_0$  to  $F_1$  could be due to other effects (e.g., material degradation and environmental effects), which were simulated in the proposed model only by accounting for the variation of  $E_c$ . However, the aim of the proposed ML model is exactly that of avoiding complex simulations while predicting overall prestressing load effects through a simple and effective tool.

On this basis, the first step for model generation is to define  $E_c$ ,  $F_0$  and a fixed external load to compute strain increments  $\Delta\epsilon_{model}^{(i,j)}$  due to the application of fixed external load itself while the considered prestressing force is constant. To this scope, the analysis is divided into two steps: (a) application of self-weight load (e.g., dead),  $F_0$  and related sectional moments; (b) application of the external load on the deformed configuration attained at the end of step (a). In both steps, geometric nonlinearities (i.e., P-Δ) are considered, solving then the equilibrium equations in the deformed configuration of the structure. According to this approach, the output of the analysis is the strain increment  $\Delta\epsilon_{model}^{(i,j)}$  which for the  $j^{th}$  generic fiber of the  $i^{th}$  section can be computed as follows:

$$\Delta\epsilon_{model}^{(i,j)} = \epsilon_{(b)}^{(i,j)} - \epsilon_{(a)}^{(i,j)} \quad (1)$$

where  $\epsilon_{(a)}^{(i,j)}$  and  $\epsilon_{(b)}^{(i,j)}$  are the absolute strain values of step (a) and step (b), respectively. The difference between  $\epsilon_{(b)}^{(i,j)}$  and  $\epsilon_{(a)}^{(i,j)}$  is required because strain values of the numerical FE model are absolute, and experimental strain measures are relative to the time in which they started measuring (after the application of the other loads).

## 2.2. Data generation

To consider the uncertainties related to input values  $F_0$  and  $E_c$ ,

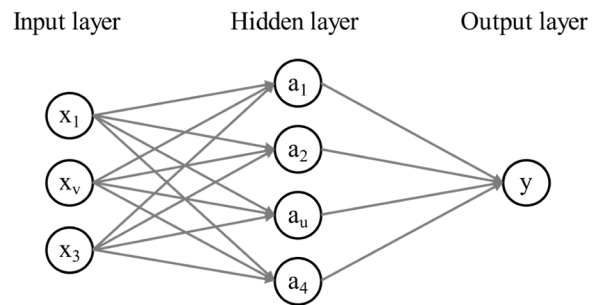


**Fig. 2.** ANN architecture.

different strategies could be used. If available, literature-based continuous distributions could be adopted (e.g., normal, lognormal) and sampling techniques could be used (e.g., see [23]), while in the case of missing information, a range of values can be accounted for by considering uniform distributions [66]. The values to consider should be characterized by physical sense, to characterize a likely sample data for training and testing the ML algorithm. Starting from a generic value of  $F_0$ , defined as "initial state" (i.e., at the time of onsite strain-sensors installation), the results of the analyses given a fixed external load can be stored,  $\Delta\epsilon_{model}^{(i,j)}$ , with the aim to compute the strain increments  $\Delta\epsilon^{(i,j)}$ . The values of this latter at different sections are calculated under the initial assumption that  $F_1 = F_0$ , simulating the case in which no prestressing force reduction occurs. Hence, values of  $\Delta\epsilon^{(i,j)}$ , which is the input of the ML algorithms, can be computed as:

$$\Delta\epsilon^{(i,j)} = \Delta\epsilon_{F_1}^{(i,j)} - \Delta\epsilon_{F_0}^{(i,j)} \quad (2)$$

where  $\Delta\epsilon_{F_k}^{(i,j)}$  is  $\Delta\epsilon_{model}^{(i,j)}$  derived by Eq. (1) under a  $F_k$  value, and  $\Delta\epsilon^{(i,j)}$  is equal to 0 for each  $j^{th}$  fiber of each  $i^{th}$  section of the model. After defining the "initial state",  $F_0$  is then reduced up to a desired percentage value, with the aim of defining different prestressing force reduction  $F_1$ . The maximum reduction rate of  $F_0$  should be calibrated case-by-case, considering the demand to capacity ratio of the structure [23]. In the end, it is worth specifying that to efficiently use the proposed method in practical applications, the input parameters at the "initial state" are needed. To this scope, onsite tests are required, both destructive and non-destructive, to determine  $E_c$  and  $F_0$  at the time of onsite strain-sensors installation, which can be evaluated by compression tests on drilled concrete cores, reduced in number by non-destructive tests, such as by employing the SonReb method. The latter, on the other hand, can be evaluated by saw-cuts tests [67] and/or static deflection measurements [45].

## 2.3. ML surrogate model

Once sample data is ready, a ML regression model can be trained to find the best relation between the input vector of  $F_0$ ,  $E_c$ , and  $\Delta\epsilon^{(i,j)}$ , and the output value,  $F_1$ . Different viable options can be employed, according to the available ML algorithms in the literature. This Section presents a brief description of the selected candidates for defining the proposed ML surrogate model. Three main ML algorithms were adopted in this study: ANN, RFR, and SVR. ANN was selected for its ability to generalize problems, even though it presents many hyperparameters to be tuned. RFR is robust against overfitting and is simpler to set, given a smaller number of overall hyperparameters. SVR is a sort of compromise between ANN and RFR, because it is robust against overfitting but, at the same time, challenging in hyperparameter tuning [58].

Going into detail, ANN is a computational model inspired to the human brain, and it is used for tasks such as pattern recognition, data classification, and predictive analytics. A typical ANN, shown in Fig. 2, is characterized by layers, and for each layer, one or more nodes (neurons) can be observed. The input,  $[X] \in \mathbb{R}^{nx1}$ , and output,  $[Y] \in \mathbb{R}$ , layers are

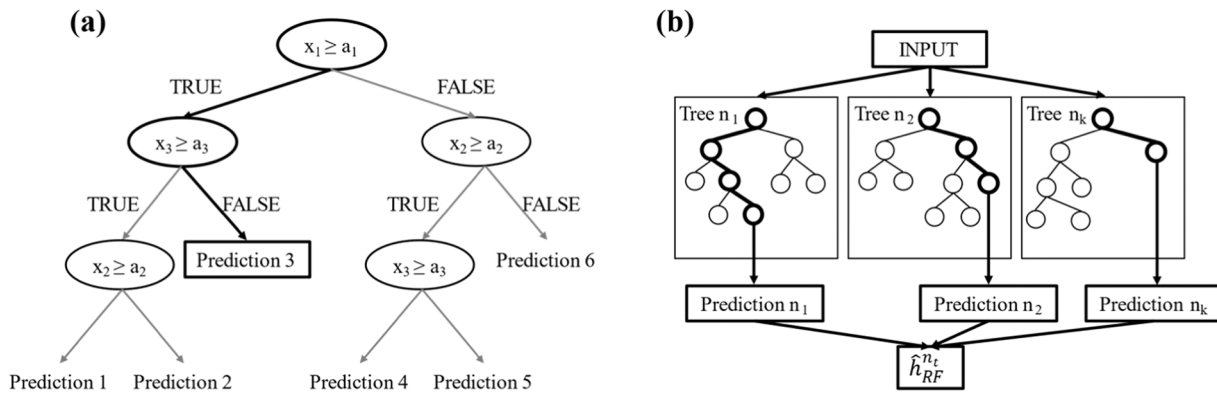


Fig. 3. (a) Example of Decision Tree and (b) Random Forrest Regressor architecture.

described with a number of neurons equal to the input,  $x_v \in [X]$ , and output values,  $y \in [Y]$ . Between the extreme layers, one or more hidden layers can be involved, able to perform the intermediate calculations and establish the relationship. All nodes of each layer are connected to all nodes of the subsequent layer, and for each connection, a specific weight is assigned. The special feature of ANN is the activation function,  $\psi$ , which transforms the output of the neuron,  $a_u$ , by inserting some nonlinearities depending on the specific application (e.g., Sigmoid, Tanh, ReLU). Looking at ANN in Fig. 2 with  $n$  equal to 3:

$$a_u = \psi\left(\sum_{v=1}^n (w_v \cdot x_v) + b_u\right) \quad (3)$$

where  $w_v \in [W_1]$ ,  $[W_1] \in \mathbb{R}^{1 \times n}$  is the weight associated to  $x_v$  and  $b_u \in \mathbb{R}$  is the bias associated with the activation of the neuron. In matrix form, considering all the “ $m$ ” neurons in the hidden layer:

$$[A] = \psi([W_1] \bullet [X] + [B]) \quad (4)$$

where  $[W_1] \in \mathbb{R}^{n \times m}$ ,  $[B] \in \mathbb{R}^{m \times 1}$  and  $[A] \in \mathbb{R}^{1 \times m}$ . To proceed to the output layer, each  $a_u$  value of  $[A]$  matrix is weighted again via another weight matrix,  $[W_2] \in \mathbb{R}^{m \times 1}$  and the output  $y$ , according to the input vector  $[X]$ , is equal to:

$$y = [W_2] \bullet \psi([W_1] \bullet [X] + [B]) \quad (5)$$

The performance of the ANN is evaluated through a loss function, selected depending on the application (see Section 2.4), whose value is computed at each epoch after updating the weights and bias values through an optimization algorithm (e.g., Gradient descent, Stochastic Gradient Descent, Adam). The use of ANN is justified for the ability of this model to generalize problems (for the case at hand, an ANN with 2 hidden layers was selected [56]), even though many hyperparameters should be tuned, such as training epochs and batch size. Training epochs represent the number of epochs to train a model, while batch size is the number of samples per batch of computation. Higher values of the above hyperparameters require higher computational resources. To determine the optimal set of hyperparameters ensuring the best performance of the model and avoiding overfitting problems, the grid search approach with 10 k-fold cross-validation can be implemented [57,68].

Random Forrest (RF) algorithms, first proposed by Breiman [69], are ensemble learning methods designed for both regression and classification. RFR is an extension of RF algorithms, typically applied for classification problems and useful for predicting numerical output. RFR, shown in Fig. 3(b), is a meta estimator employing different Decision Tree (DT) regressors (see Fig. 3(a)) on various sub-samples of the dataset and uses averages to improve the predictive accuracy and control overfitting [70]. A DT is a nonparametric regression approach, which generates a tree-like graph composed of a root node, internal nodes and leaves. The root node contains the sub-sample of data, the internal nodes represent the points in which the dataset is split in  $u$  distinct and

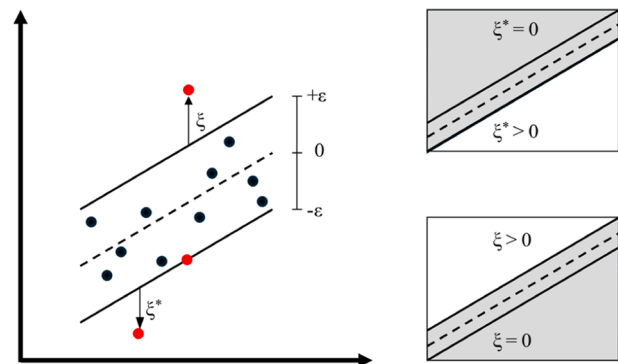


Fig. 4. Schematic representation of SVR.

nonoverlapping regions  $R_u$  based on certain features and criteria by minimizing a loss function (e.g., Root Mean Squared Error, RMSE). Leaves (or terminal nodes) are the points reporting final output values for the predictions, assumed equal for each observation falling in the  $R_u$  region.  $R_u$  is determined through an iterative process (recursive binary splitting) and the minimum size node is the hyperparameter governing the subdivision. When a node exceeds the minimum size, it can be defined as an internal node, otherwise, it is a leaf. This workflow is called top-down strategy [71] and in this way, DT can make the prediction by following the path from the root note to the leaves. From the mathematical point of view, the output of the RFR,  $\hat{h}_{RF}^{n_t}$ , can be expressed by the following equation:

$$\hat{h}_{RF}^{n_t} = \frac{1}{n_t} \bullet \sum_1^{n_t} h_{n_t}(x) \quad (6)$$

where  $h_{n_t}(x)$  is the individual prediction of a tree,  $n_t$ , for an input vector  $x$ . As for ANN, hyperparameter tuning is required considering the number of trees in the Forrest, maximum number of levels in each decision tree, and minimum number of data points placed in a node before splitting.

SVR, reported in Fig. 4, is a specific type of Support Vector Machine [72], which is adequate for predicting continuous numerical values [73]. SVR is built from training data, and it employs a regression function,  $f$ , to map training data as closely as possible to the numerical output labels. For nonlinear regression tasks, given a set of  $z$  training data  $T$ , where  $T = \{(x_c, y_c)\}_{c=1 \dots z}$ ,  $x_c \in \mathbb{R}^n$ ,  $y_c \in \mathbb{R}$  and a set of functions  $F$  with  $Z$  set of parameters, where  $F = \{f(x, \alpha), \beta \in Z | f: \mathbb{R}^n \rightarrow \mathbb{R}\}$ , the regression function can be expressed as:

$$f(x, \alpha) = \beta \bullet \varphi(x) + b \quad (7)$$

where  $\varphi$  is a nonlinear function to linearly map input space into a high-

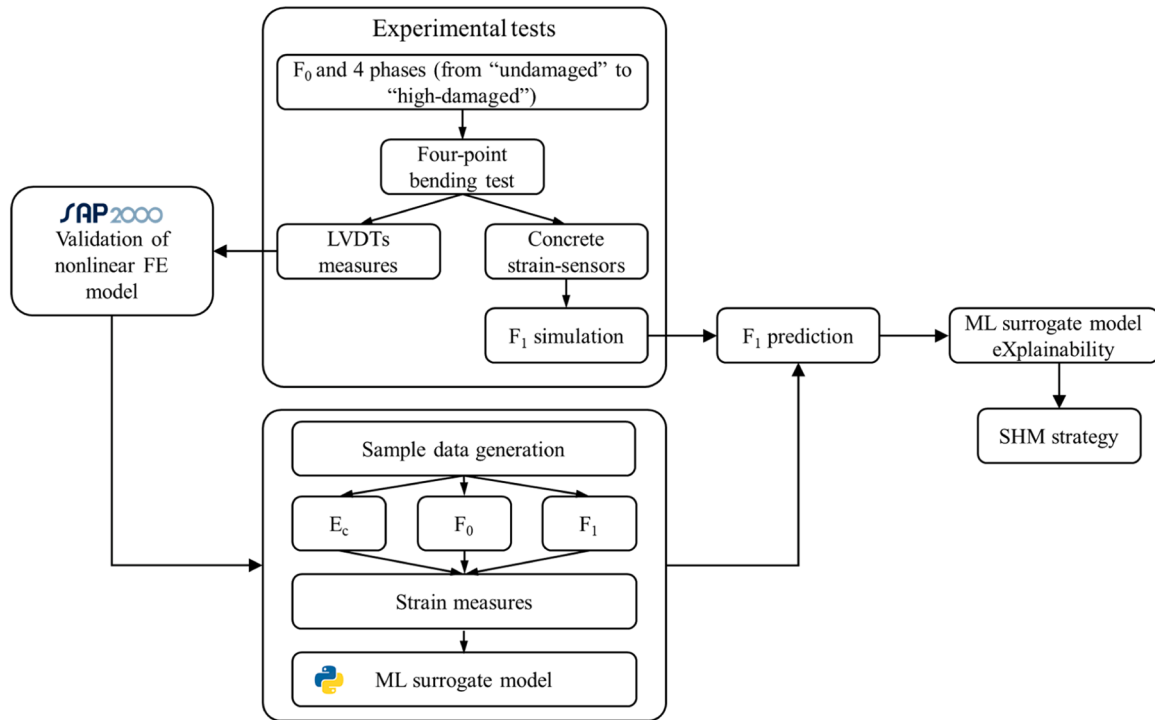


**Fig. 5.** Framework application on an experimental case.

dimensional feature space. If the error between predicted and real values is lower than  $\varepsilon$ ,  $f$  can predict  $y$  correctly.  $\beta$  is the optimal separating hyperplane in SVR according to a minimization function:

$$\min \frac{1}{2} \|w^2\| + C \frac{1}{l} \sum_{c=1}^z V(x, y, f) \quad (8)$$

where  $V(x, y, f)$  is Vapnik's  $\varepsilon$ -insensitive loss function:

$$V(x, y, f) = \begin{cases} 0 & \text{if } |f(x) - y| \leq \varepsilon \\ |f(x) - y| - \varepsilon & \text{if } |f(x) - y| > \varepsilon \end{cases} \quad (9)$$

which is employed to find a function that fits the current training data with a deviation less than or equal to  $\varepsilon$ , under these constraints:

$$\begin{cases} \beta \cdot \varphi(x) + b - y_c \leq \xi_c^* + \varepsilon \\ y_c - \beta \cdot \varphi(x) - b \leq \xi_c + \varepsilon \\ \xi_c, \xi_c^* \geq 0 \end{cases} \quad (10)$$

The terms  $\xi_c$  and  $\xi_c^*$  are defined as slack variables, which denote the excess deviation in the upper and lower regions outside support vectors (Fig. 4). The differences between prediction and real values are constrained in a region defined by the  $\varepsilon$  hyperparameter. Thus,  $\varepsilon$  can be considered as a tolerance, and only predictions characterized by a residual greater than  $\varepsilon$  are penalized. The data on and outside the  $\varepsilon$ -boundary are called support vectors.  $C$  is a positive constant that defines the degree of penalization when a training error occurs. For large values of  $C$ , a complex model is obtained, able to avoid training errors with the risk of overfitting, while a small value of  $C$  leads to a model characterized by low complexity with a tendency to insufficiently fit training data [74,75]. Hence, the tuning of the  $C$  hyperparameter is critical for achieving a compromise between model accuracy and generalizability. Finally, the kernel function is involved together with the method of Lagrange to express the prediction function (e.g., radial basis kernel function). As for ANN and RFR, hyperparameter tuning is required starting from  $C$ ,  $\varepsilon$  and kernel.

#### 2.4. Evaluation metrics and eXplainability approach

The selection of a specific algorithm for the definition of the proposed ML surrogate model depends on the higher prediction accuracy provided by each proposal. The predictive accuracy of the models can be assessed through the definition of some statistical metrics: coefficient of determination ( $R^2$ ), Mean Squared Error ( $MSE_1$ ), RMSE, Mean Signed Error ( $MSE_2$ ) and Mean Absolute Error (MAE), defined as:

$$R^2 = 1 - \frac{\sum_{m=1}^p (y_m - \bar{y}_m)^2}{\sum_{m=1}^p (y_m - \mu_e)^2} \quad (11)$$

$$MSE_1 = \frac{1}{p} \sum_{m=1}^p (y_m - \bar{y}_m)^2 \quad (12)$$

$$RMSE = \sqrt{MSE_1} = \sqrt{\frac{1}{p} \sum_{m=1}^p (y_m - \bar{y}_m)^2} \quad (13)$$

$$MSE_2 = \frac{1}{p} \sum_{m=1}^p |y_m - \bar{y}_m| \quad (14)$$

$$MAE = \frac{1}{p} \sum_{m=1}^p |y_m - \bar{y}_m| \quad (15)$$

where  $p$  is the number of data points,  $y_m$  is the experimental value,  $\bar{y}_m$  is the predicted value,  $\mu_e$  is the average value of experimental values.

Generally,  $R^2$  expresses the correlation among variables, and it is used to evaluate the goodness of fit of a regression model.  $MSE_2$  describes the mean of the distances between experimental and predicted regression model values, and it accounts for the sign of the error. RMSE is the root of  $MSE_1$  and presents the main advantage to be in the same unit measure of the response variable (in this sense, RMSE is preferred to  $MSE_1$  for its straightforward interpretability). While higher values of  $R^2$  are preferable, the fitting is more accurate if lower values of RMSE are obtained. Regarding  $MSE_2$ , it is not possible to define an optimal value, but a positive value leads to underestimate the ground truth and vice

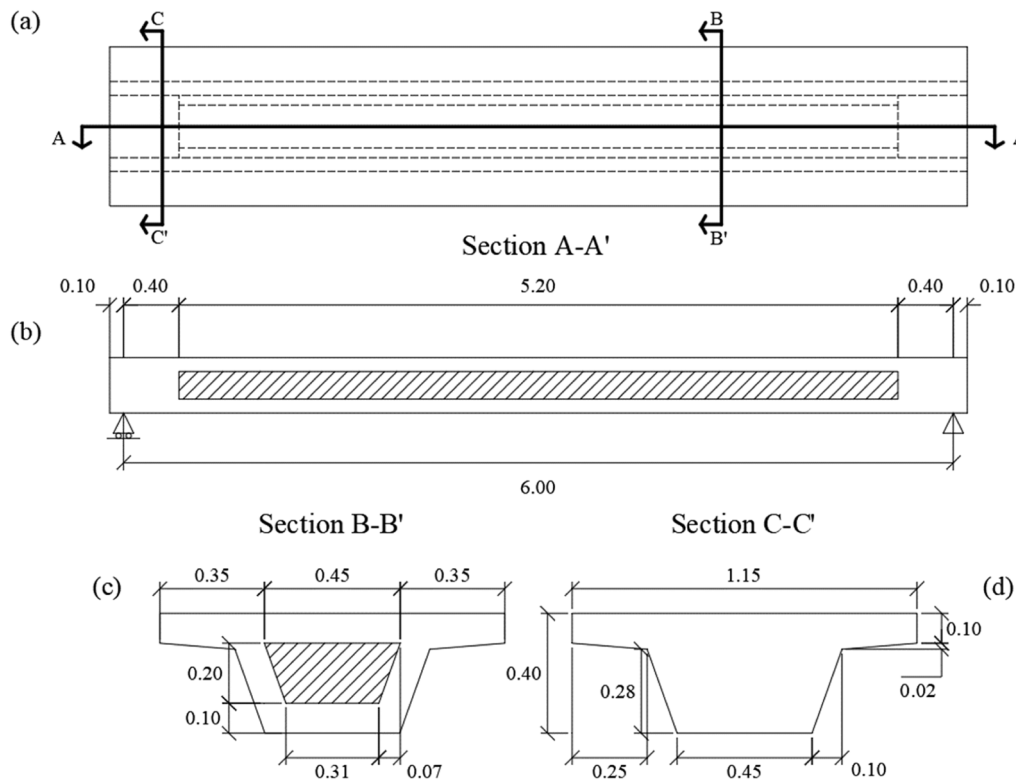


**Fig. 6.** Geometry of lab-tested scaled PSC box bridge: (a) Top view, (b) Longitudinal section A-A', (c) Hollow cross-section B-B', (d) Solid cross-section C-C'.

versa. Finally, MAE provides a more balanced representation of errors, considering the combination of positive and negative errors in absolute value. This makes MAE a robust choice when the direction of errors is not critical. For the case at hand, the discriminant metrics for selecting the ML surrogate model is the MSE<sub>2</sub>. In fact, it is important to distinguish between positive and negative errors, because a smaller value of  $F_1$  is conservative, reflecting then a positive value of the error. On the other hand, RMSE is the best way to compare the accuracy of ML models, because as above reported, it is an overall metrics able to give an idea about the obtained output, in the same unit measure of the output itself.

Finally, given the nature of the proposed black-box models, a physical explanation of ML surrogate model can provide additional insights into the prediction. To this scope, eXplainability metrics could be exploited. Although different eXplainability techniques are available in the literature, a viable option is a model-agnostic interpretable method, such as SHAP, [61]. This latter can be used to deeply investigate the structure of ML models by analysing the relationship between the input variables and output of the model (called SHAP value). SHAP uses cooperative game theory to allocate credit for a model output among its input features. The idea is to consider each feature as a player and the dataset as a team. The players give their contribution to the result of the team. The influence of a feature is dependent on the complete set of features in the dataset and not on only a single feature. Thus, SHAP retrains the model overall feature combinations accounting for the feature under consideration, by calculating SHAP value using combinatorial calculus. The significance of a feature can be determined by estimating the average absolute value, which is compared with a target variable.

$$\gamma_o(\delta, r) = \sum_{S \subseteq N \setminus \{o\}} \frac{|S|!(|N| - |S| - 1)!}{|N|!} [\delta_r(S \cup \{o\}) - \delta_r(S)] \quad (16)$$

Eq. (16) describes mathematically the SHAP value,  $\gamma_o$ , of the input feature  $o$ .  $\delta$  is the trained ML model,  $r$  is a generic record of the sample data,  $N$ , and  $S$  is a subset of  $N$  that does not include  $o$ . The two terms

under the summation sign express the weighting function for the impact on each subset of features  $S$ , and the impact of removing the feature  $o$ , respectively. For the case at hand, the importance of SHAP application is dual: (i) SHAP can highlight which parameters require an accurate evaluation because they present a higher impact on the output values; and (ii) SHAP can indicate the best combination of fibers and section to monitor based on significance of features, to reduce the cost of the sensors-based system to design.

### 3. Experimental tests on a scaled psc box bridge and results

The framework described in Section 2 was applied to an experimental case study, and the steps performed are summarized in Fig. 5.

#### 3.1. Description of the specimen

The considered specimen was a scaled PSC box-girder bridge tested in the ICITECH laboratory of the *Universitat Politècnica de València* [76]. The use of a scaled model is justified by the necessity to simulate the prestressing loss in a controlled environment, besides the impossibility to create a real dimension specimen in laboratory or to produce controlled damage in a real bridge under service. At the same time, the investigation of one (or more) full-scale specimen would allow the generation of more reliable data in the next steps of the work. The specimen, shown in Fig. 6, is geometrically defined as a box-girder having length,  $L$ , equal to 6 m, supported by two hinged and a hinged-roller supports (see Fig. 6, right and left respectively). At both beam ends, the box section is solid for a length of 0.40 m (Fig. 6(d)), while in the middle the box section is lightened by expanded polystyrene (Fig. 6(c)). During the construction phase, three polyvinyl chloride tubes, diameter of 24 mm, were placed in the bottom part of the section, to subsequently insert unbonded prestressing bars. Given the use of a scaled model, it was not possible to reproduce a prestressing system like the one employed in real bridges, but tendons were simulated by three steel bars with 20 mm of diameter. The bars, 45 days after concrete

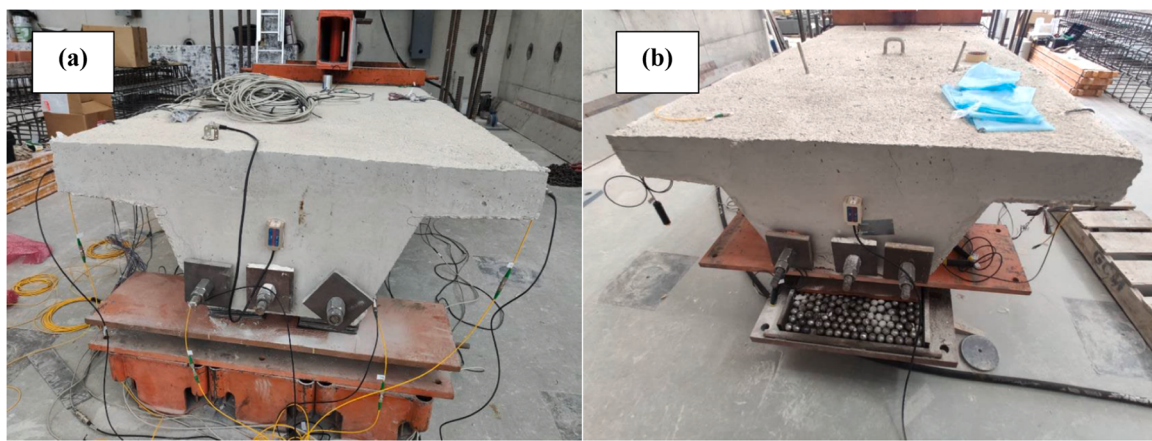


**Fig. 7.** View of anchorages of prestressing bar on (a) fixed and (b) mobile support.

**Table 1**

Results of mechanical tests through Ibertest universal machine, on nine concrete cylinders, three investigated after 14 days and three investigated after 45 days.

Compressive strength [MPa]	Tensile strength [MPa]	Elastic modulus $E_c$ [MPa]
14 days	45 days	45 days
29.86	34.99	39464
29.28	31.34	36741
Discarded value	32.12	32412

casting, were placed into the housing and were anchored through bolts with steel plates interposed to the end faces of the beam after stringing operations, as shown in Fig. 7. Regarding construction materials, the concrete class used was C30/37 (according to Eurocode 2 [65]) with aggregates having maximum size of 20 mm, while steel used for both mild and prestressing reinforcement was B500C [65]. Mechanical properties of the concrete, compressive and tensile strength and  $E_c$ , were evaluated through tests on nine cubic specimens collected before casting the main specimen. Regarding concrete curing, both concrete specimen types were subjected to pouring water for the first three days after casting and, before performing mechanical tests, no shrinkage cracks were detected. The mechanical properties of concrete were evaluated 45 days after concrete casting, rather than 28 days as usual in the practice, to provide a representative description of the mechanical features of the specimen during the Four-point bending tests, which were carried out on the same day of the stringing operation of prestressing bars. On the other hand, the mechanical properties of the steel were assumed equal to the ones declared by the manufacturer (i.e., see mechanical properties of B500C steel, as reported in the Eurocode 2 [65], with yielding and ultimate strength equal to 500 and 620 MPa, respectively, and ductility factor equal to 1.24). Test results of concrete tests are summarized in Table 1.

After defining the specimen, the beam was instrumented for two main reasons: (i) to calibrate a nonlinear FE model; (ii) to record strain measurements while simulating prestressing losses. Regarding the adopted monitoring system, several sensors were installed as shown in Fig. 8: (i) ten linear variable displacement transducer (LVDTs) were placed along the longitudinal development of the beam, one for each meter starting from the mobile support and considering both left and right side of the section, to measure the vertical displacements (Fig. 8 (b)); (ii) twenty-one embedded strain gauges to monitor concrete deformations, subdivided among five placed on lower part of the section at two different cross-sections, glued to the bottom rebars and located at the middle, at a quarter of the span length ( $L/4$  and  $L/2$ , which is 1.5 m and 3 m from the hinged support, respectively), and at mobile support, for a total of fifteen sensors (Fig. 8(c)); and three placed on each side of every prestressing steel bar to measure deformations and to derive both

axial stress and prestressing force during stringing operations and investigation phases (i.e., Four-point bending test), for a total of six sensors (Fig. 8(d)). Although strain sensors are usually placed on the bottom and upper fibers of the same section, the selected location of the sensors was an engineering choice since, for the type of loading, the main strain increments were expected in the considered positions. In addition, a FBG sensor was placed for the entire length of the bridge, in the same vertical position of strain sensors and in the upper face to provide strain increments on top fibers. According to the definition of the specimen, the value of prestressing force applied to each bar was equal to 110 kN (and then,  $F_0$  was equal to 330 kN), which resulted in a stress on each bar equal to 350 MPa.

The final value of  $F_0$  also included the instantaneous prestressing losses due to the elastic deformation of the concrete induced by the sequential strand stringing. It is worth noting that due to the application of the prestressing force and the performance of the entire experimental campaign on the same day (i.e., the 45th day after the concrete casting), the early-age phenomena due to relaxation of the tendons and creep can be considered negligible.

### 3.2. Experimental setup and test

The laboratory tests were designed to assess the effects of prestressing variation due to the loss of functionality of steel strands on the box beam deformations through strain gauges. To this scope, the experimental campaign was subdivided into four phases: Phase 1, also named “undamaged”, in which the beam was loaded in its initial state; Phase 2, also named “low-damaged”, in which the prestressing loss was simulated by removing one of the three bars and the same loading was performed again; Phase 3, also named “moderate-damaged”, in which the prestressing loss was simulated by removing an additional bar (two of the three bars are removed) and the same loading was performed again; Phase 4, also named “high-damaged”, in which the loss of the whole prestressing force was simulated by the removal of the three post-tensioning bars and the same loading protocol was performed. For all cases, the loading was applied through a Four-point bending test in which the maximum applied load was set to 140 kN for Phases 1, 2, 3 and 4, although the test continued until failure in Phase 4, reaching a final value of load equal to 210 kN. The setup of the tests can be observed in Fig. 9, while schematic test configuration in terms of geometry and loading steps is shown in Fig. 10. In Fig. 11, the end sections in the four considered Phases are illustrated, with the progressive removal of the prestressing bars. The loading protocol and the test were designed to ensure a quasi-elastic behaviour of the specimen from Phase 1 “undamaged” to Phase 3 “damaged”, where also damage was incremental to avoid a significant effect of one test on the subsequent one. In addition, over the first three phases, the specimen did not exhibit either

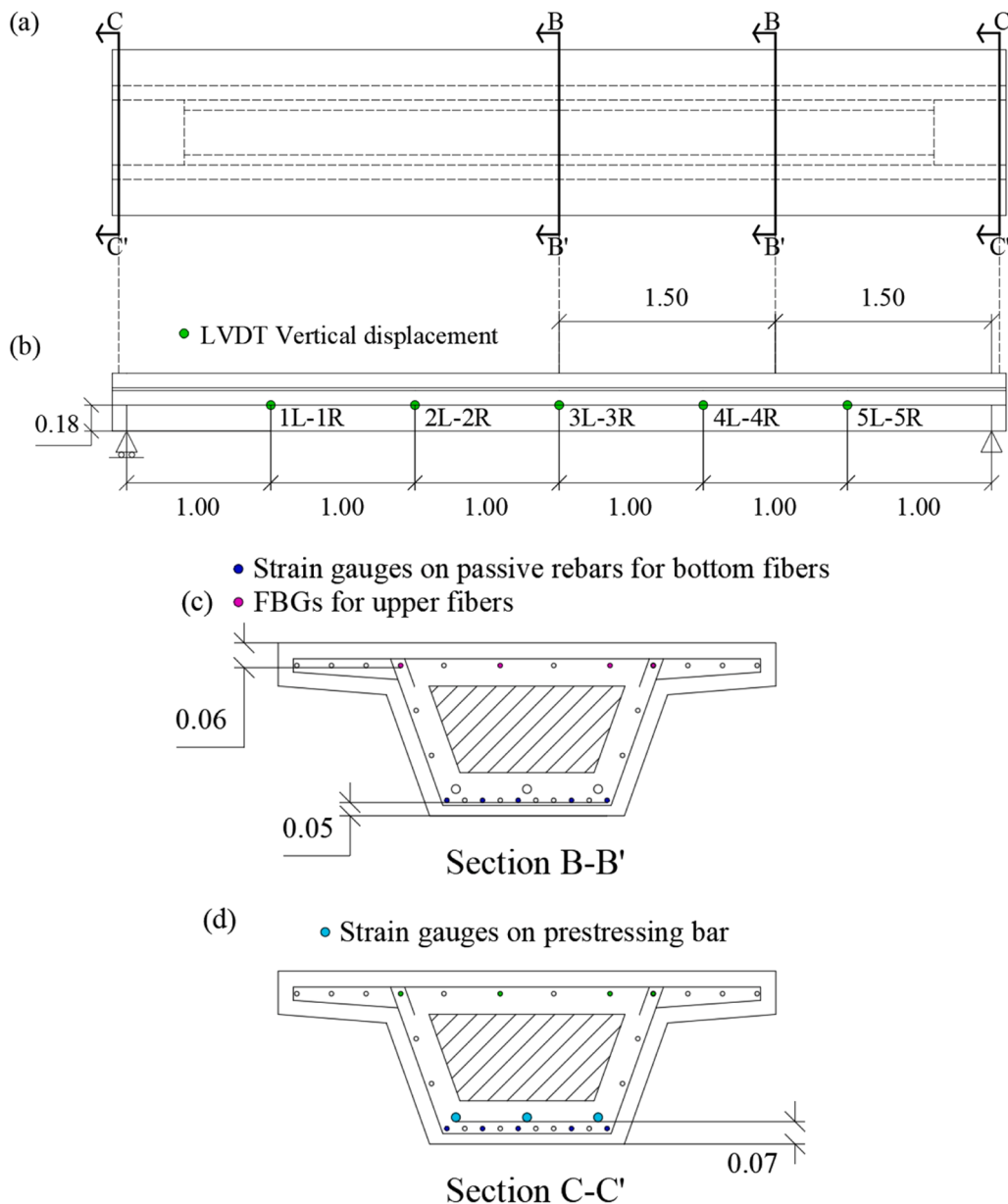


**Fig. 8.** Position of installed sensors: (a) Top view, (b) Longitudinal view on left side, (c) Hollow cross-section B-B', (d) Solid cross-section C-C'.



**Fig. 9.** Set up of the Four-point bending test.

vertical cracks in the middle due to bending moment or residual displacements due to plastic deformation of materials. The absence of residual plastic deformation was verified by comparing sensor measurements at the beginning and at the end of the loading-unloading protocol of each phase, not observing differences in terms of deformation. Effects like creep, shrinkage, and strand relaxation were not considered, for the reasons reported in Section 3.1 (the application of the prestressing force and the entire experimental campaign were performed on the same day, minimizing the effects of early-age phenomena). In addition, considering the bridge typology under investigation, the effect of aging should reflect also the contributions of relaxation phenomena. At the end of each Phase, the values of  $\Delta\epsilon^{(i,j)}$  were recorded, in the positions where the strain gauges were located.

### 3.3. Definition and calibration of the FE model

Having at disposal the data about experimental tests, a nonlinear numerical FE model of the specimen was carried out, by calibrating to the numerical output on the vertical displacements measured with LVDT

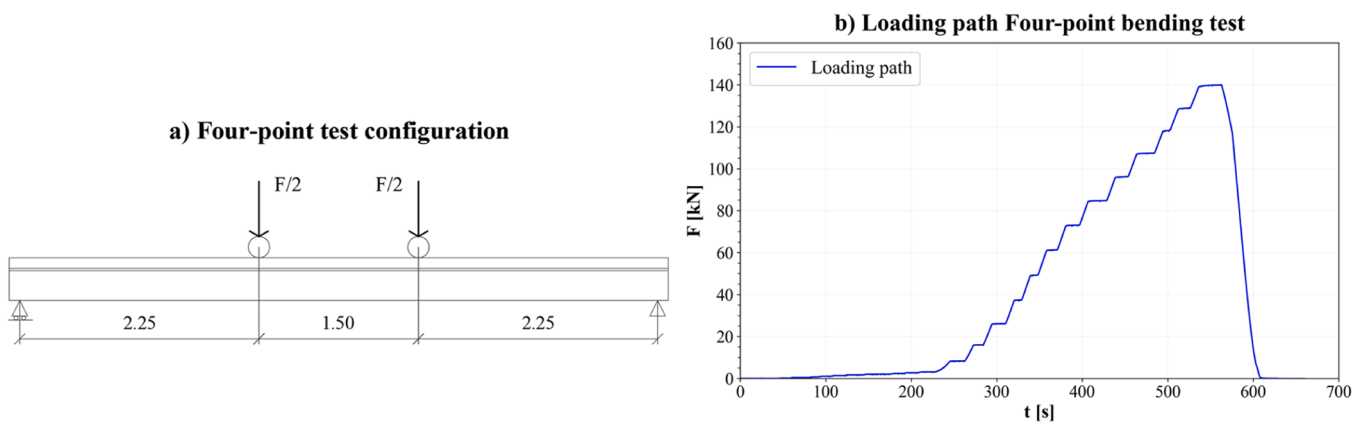


Fig. 10. Four-point bending test: (a) configuration ( $F/2$  indicates half of the total force applied in those positions); (b) loading protocol of Phase 1.

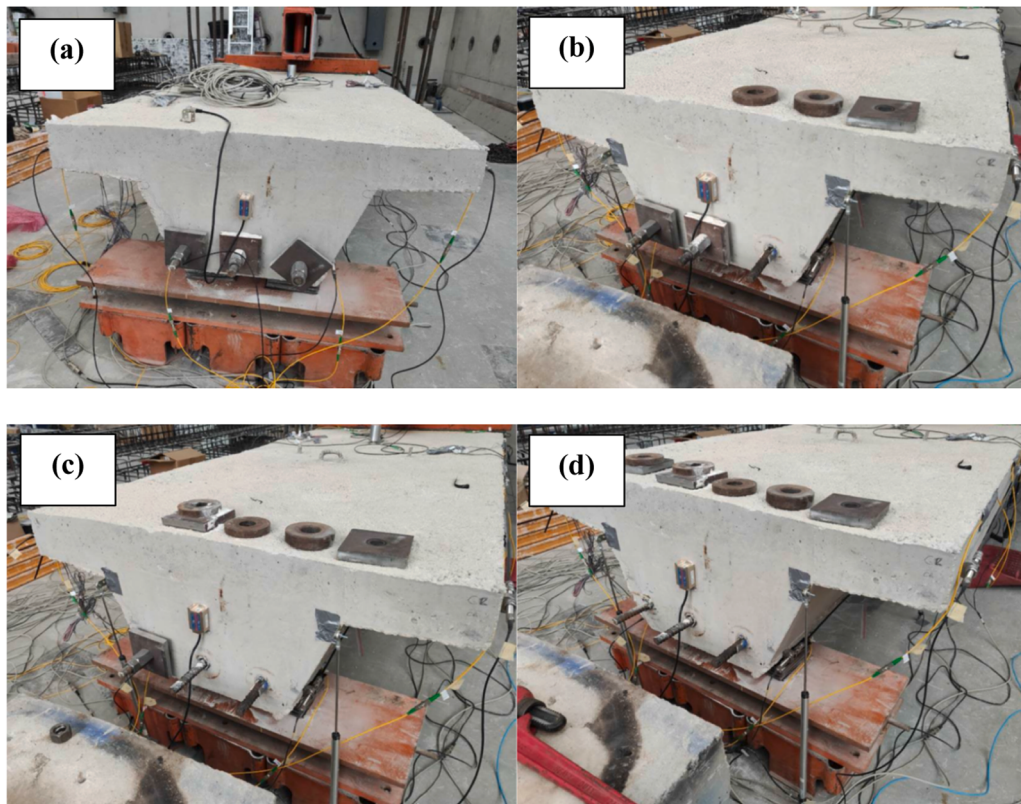
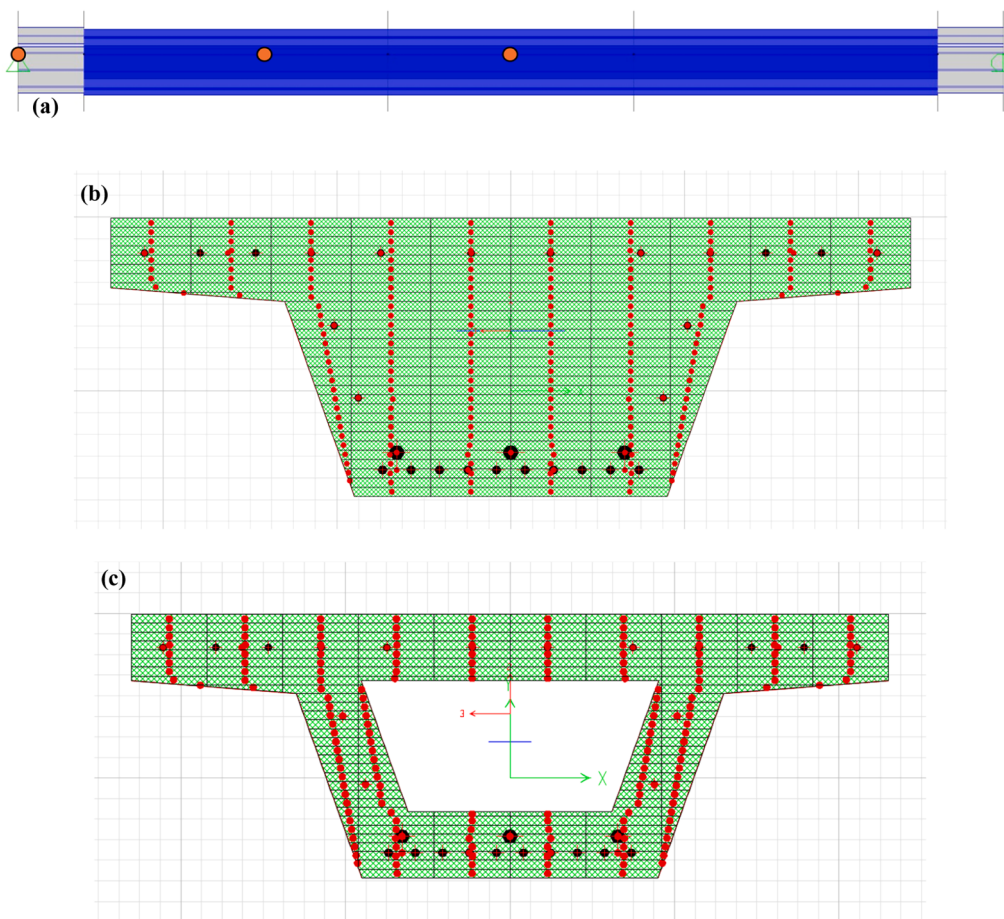


Fig. 11. End section of the box-girder specimen, observed at Phase 1 (a), Phase 2 (b), Phase 3 (c) and Phase 4 (d).

sensors. The bridge was simulated through the SAP2000 structural software, v.25 [77], by using frame elements. The girder was divided in five frame elements of different length. The two external frames, indicated with grey elements in Fig. 12(a), were characterized by a solid cross-section, Fig. 6(c) and Fig. 12(b), with a length 0.40 m. The three central frames, indicated with blue elements in Fig. 12(a), were characterized by a hollow cross-section, Fig. 6(d) and Fig. 12(c), with different lengths of 1.85 m, 1.50 m, and 1.85 m, respectively. The subdivision of the central part was set to simulate the position of the vertical loads of the Four-point bending test. External restraints were assigned to the external frames to simulate supports with proper degrees of freedom (i.e. one hinge and one hinged-roller supports).

Regarding the load applications, as schematically reported in Fig. 10 (a), the loads were applied at a 2.25 m distance from the supports. Still, considering the frame a one-dimensional element, the vertical load

condition of the four-point test was modelled by two vertical forces, whose values were half of the experimental load (i.e., 70 kN for 140 kN load step of Phase 1 “undamaged”). The axial load of the prestressing system was applied on both the sides of the beam (110 kN for each bar depending on the phase under investigation), accounting for bending moments due to the eccentricity with respect to the centroid of the section (red local reference system in Fig. 12(c)), indicated with  $M_x$  and  $M_y$  around X and Y axes, respectively (see green reference system in Fig. 12(c)) [64]. Indeed, the prestressing bars were placed at a distance equal to 0.19 m and 0.18 m from the centroid of the section in the Y direction (green reference system in Fig. 12(c)) for hollow and solid section, respectively. Given the different position of the centroid for the two sections, an additional bending moment was considered at the end of frames with hollow cross-section in the FE model. Moreover, when simulating Phase 2 “low-damaged” and Phase 3 “moderate-damaged”,



**Fig. 12.** FE model in SAP2000: (a) frame elements of the FE model with plastic hinges (orange dots); (b) solid cross-section fiber definition; (c) hollow cross-section fiber definition.

the absence of one or more prestressing bars generated an additional bending moment around the Y axis, which was applied only at the end of frames with solid section (considering that the centroid of the two sections differed only in the Y direction).

Concerning the nonlinear modelling, the diffused plasticity strategy mentioned in Section 2.1 regarded the number and distribution of plastic hinges in the beam (PMM type due to the interaction of prestressing force and bending moments). The behaviour of the plastic hinges was defined by the software considering the section, fibers and mechanical properties of materials. Solid and hollow cross-sections were divided as 10 fibers in X direction and 30 in the Y direction (see Fig. 12 (c)) for a total number of 235 and 207 fibers, respectively. The selected number of fibers was fixed according to two main considerations: (a) the differences in terms of strain, obtained with a model characterized by a higher number of fibers than the current model, were lower than 5 %; (b) the discretization in fibers was set to match the position of strain gauges. Thus, plastic hinges were placed at girder mid-length (i.e., at 3.0 m) and at a distance equal to 1.5 m from hinged support for the hollow section, and at the end of the beam for the solid section near the hinged support. The analysis on the FE model was subdivided into two steps: (i) application of external forces due to the prestressing system (i.e., axial loads and bending moments); (ii) application of Four-point bending test load in a force-controlled approach on the geometric configuration of the step (i). Both analyses considered geometrical nonlinearities (i.e., P-Δ).

The numerical calibration was performed by varying only one parameter, that is, the  $E_c$  value. To assess the accuracy of the numerical model, several comparisons between numerical and experimental results were performed. Vertical displacements were compared for each

Phase using LVDT records on the left and right part of the box-girder. As for example, Fig. 13 reports the comparison between experimental and numerical results in Phase 1 (i.e., “undamaged”) and in Phase 2 (i.e., “low-damaged”), both for an intermediate load step of 60 kN, and for the last load step of 140 kN. As can be observed, there is a total agreement between numerical and experimental results, with low percentage differences both in the “undamaged” and “low-damaged” cases. Numerical results can be also checked in Table 2, where the differences both in percentage values and in millimetres for the ten LVDTs placed on the beam are reported. In detail, the experimental vertical displacements are higher than the numerical ones on average by 1.4 % and 0.8 % in Phase 1 (“undamaged”) and Phase 2 (“low-damaged”), respectively, for a load step of 60 kN, and on average by 1.2 % and 0.7 % on Phase 1 (“undamaged”) and Phase 2 (“low-damaged”), respectively, for a load step of 140 kN. This is an important achievement since confirms and justifies the type of simplified nonlinear numerical model used for the next steps.

The same conclusion can be drawn by comparing experimental and numerical values of stress levels of prestressing bars during Phase 1, Phase 2, and Phase 3. Stress values were derived from strain measures and were equal to 429 MPa, 459 MPa and 493 MPa for Phase 1 “undamaged”, Phase 2 “low-damaged”, and Phase 3 “moderate-damaged”, respectively (considering an initial stress value of 350 MPa at the bar straining). During Phase 4 “high-damaged”, stress values were available only for mild reinforcements, which were beyond the yielding tensile strength of steel, i.e., 500 MPa. The above values were assessed also in the FE model, and a good agreement in terms of stress was observed, with a percentage difference of 2 % on average.

Looking at the results in Fig. 13, it is worth noting that the values

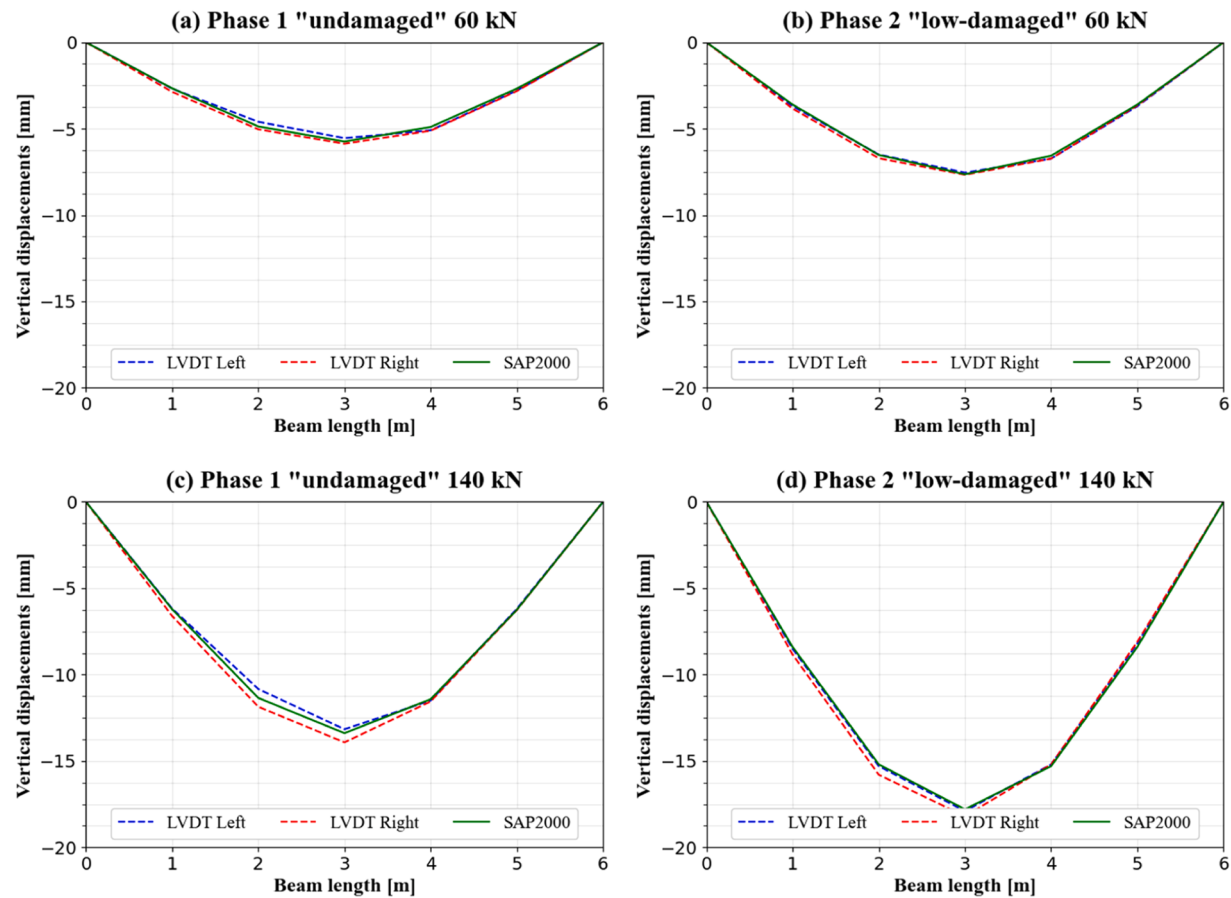


**Fig. 13.** Comparison between numerical (step (ii) SAP2000) and experimental (Phase 1 “undamaged” and Phase 2 “low-damaged” LVDT) vertical displacement values for 60 kN (a – b) and 140 kN (c – d) steps. All the values are expressed in millimetres; therefore, all vertical deformed shapes are in 1000:1 scale with respect to beam length.

obtained by the numerical FE model are equal on the left and right sides, considering that the structure was modelled as a frame element. In addition, the calibration performed with a “trial-and-error” approach showed that the value of  $E_c$  was equal to 38150 MPa, which is in good agreement with experimental data reported in Table 1 (5 % of difference with the average value of the three concrete cylindric specimens after 45 days, equal to 36200 MPa). The higher value of the calibrated  $E_c$  is balanced by the assumption of perfect external restraints, which in the FE model ensure null rotational stiffness. The balance between the ideal boundary conditions (FE model should experience higher deformations) and different mechanical properties (FE model should experience lower deformations) provided a deformation for the FE model comprised between the LVDT measurements on both sides of the beam, as shown in Fig. 13.

#### 3.4. Sample data generation

Given the calibrated nonlinear numerical FE model, new data were generated by varying some parameters in a schematic way. To this scope, SAP2000 OpenAPI was used, and, through Python programming language [78], several numerical FE models were created and analysed. The first varied parameter was  $E_c$ , which was randomly changed between 30000 MPa and 40000 MPa for 129 times (this interval of variation is justified later in this Section). After, considering the necessity to simulate the prestressing losses and the presence of three unbonded steel strands, a first hypothesis was fixed, that is, each bar was equivalent to a classical tendon made by three 7-wire strands to be able to progressively simulate the loss of a small percentage of post-tensioning. According to this assumption, the variation from  $F_0$  to  $F_1$  was simulated by

eliminating a progressive number of wires from the three available unbonded steel strands, in order to define a progressive percentage drop rate. With this regard, a minimum value of absolute percentage drop rate equal to 0 % was assumed (initial state), while a maximum value of absolute percentage drop rate equal to 40 % was fixed. Obviously, higher values of percentage drop rate could be considered but, according to the available literature (e.g., Nettis et al. [23]), a percentage drop rate of 20 % already might lead to capacity-demand ratios lower than the unity. Hence, the simulation of a prestressing loss of 40 % can be assumed double an acceptable physical limit. Besides, it is important to train the ML surrogate model for real situations and not towards extreme limits of damage that are physically admissible. In addition, a percentage drop rate of 40 % simulated a loss in  $F_0$  assimilable to the 33 % obtained in the laboratory test by removing one of the three bars (i.e. the calibration performed in this work is consistent for the creation of the ML surrogate models).

The logic behind the model generation aimed at defining different values of  $F_0$  and  $F_1$ , to cover a large range of real applications. Let us define two values of percentage drop rate: (a) initial percentage drop rate, which represents the initial prestressing loss imposed on  $F_0$  to vary this value in the ML model; (b) final percentage drop rate, which represents the final prestressing loss on  $F_0$  that provide the value of  $F_1$ . Assuming a fixed value of  $E_c$  and a value of  $F_0$  with a declared initial percentage drop rate, a progressive removal of one wire for each strand was simulated (i.e., a numerical FE model), until achieving a final percentage drop rate of 40 %. For example, if the initial drop rate is 0 %, the model is characterized by three groups of three 7-wires strands, each one containing 21 wires, and a final percentage drop rate of 40 % can be achieved when each group of three strands is characterized by 13 wires

**Table 2**

Comparison between numerical (step (ii) SAP2000) and experimental (Phase 1-undamaged and Phase 2-low-damaged LVDT) vertical displacement values for 60 kN and 140 kN steps.

Phase	Applied load [kN]	F [kN]	LVDT ID	Lab-test [mm]	SAP2000 [mm]	Difference [mm]	Difference [%]
1	60	330	1 L	-2.58	-2.67	0.09	-3.5 %
			1 R	-2.76	-2.67	-0.09	3.2 %
			2 L	-4.84	-4.87	0.03	-0.6 %
			2 R	-5.30	-4.87	-0.43	8.2 %
			3 L	-5.64	-5.75	0.11	-1.9 %
			3 R	-5.96	-5.75	-0.22	3.6 %
			4 L	-5.02	-4.90	-0.12	2.3 %
			4 R	-5.04	-4.90	-0.14	2.8 %
			5 L	-2.67	-2.68	0.02	-0.6 %
			5 R	-2.69	-2.68	-0.01	0.5 %
1	140	330	1 L	-6.18	-6.22	0.04	-0.6 %
			1 R	-6.61	-6.22	-0.39	6.0 %
			2 L	-10.84	-11.35	0.52	-4.8 %
			2 R	-11.86	-11.35	-0.51	4.3 %
			3 L	-13.17	-13.39	0.23	-1.7 %
			3 R	-13.93	-13.39	-0.53	3.8 %
			4 L	-11.50	-11.42	-0.08	0.7 %
			4 R	-11.55	-11.42	-0.13	1.1 %
			5 L	-6.19	-6.25	0.06	-0.9 %
			5 R	-6.26	-6.25	-0.01	0.2 %
2	60	220	1 L	-3.55	-3.61	0.06	-1.6 %
			1 R	-3.69	-3.61	-0.08	2.2 %
			2 L	-6.84	-6.52	-0.32	4.6 %
			2 R	-7.06	-6.52	-0.54	7.7 %
			3 L	-7.67	-7.64	-0.03	0.4 %
			3 R	-7.80	-7.64	-0.16	2.0 %
			4 L	-6.63	-6.57	-0.07	1.0 %
			4 R	-6.63	-6.57	-0.07	1.0 %
			5 L	-3.53	-3.61	0.08	-2.1 %
			5 R	-3.49	-3.61	0.12	-3.4 %
2	140	220	1 L	-8.51	-8.41	-0.10	1.2 %
			1 R	-8.84	-8.41	-0.43	4.8 %
			2 L	-15.37	-15.23	-0.14	0.9 %
			2 R	-15.87	-15.23	-0.64	4.0 %
			3 L	-17.92	-17.79	-0.14	0.8 %
			3 R	-18.23	-17.79	-0.45	2.5 %
			4 L	-15.23	-15.30	0.07	-0.5 %
			4 R	-15.20	-15.30	0.10	-0.7 %
			5 L	-8.20	-8.40	0.20	-2.4 %
			5 R	-8.13	-8.40	0.27	-3.4 %

(i.e., 9 models). If the initial drop rate is 10 %, the model is characterized by three groups of strands, each one containing 19 wires, and a final percentage drop rate of 40 % can be achieved when each group of three strands is characterized by 11 wires (i.e., 9 models). In this way, for achieving a final percentage drop rate of 40 %, the value of  $F_0$  was updated for values of initial percentage drop rate equal to 0 % (from 21 wires to 13 wires), 10 % (from 19 wires to 11 wires), 20 % (from 17 wires to 10 wires), 30 % (from 15 wires to 9 wires) and 40 % (from 13 wires to 8 wires), and the final number of models was equal to 39 (counting also the first case without first wire removal).

Combining the 39 models with 129 values of  $E_c$ , a total of 5031 models were generated (the number of  $E_c$  values was set to achieve more than 5000 models and, for each model, six values of  $\Delta\epsilon^{(i,j)}$  (for a total number of 30186  $\Delta\epsilon_{model}^{(i,j)}$ , taking the average strain values of the  $j^{th}$  fiber in the  $i^{th}$  section) were extracted (according to the locations of strain gauges and FBG sensors installed for the reference laboratory test). The generated sample of data was then used for calibrating the ML surrogate model. In literature, the size of the sample data varies and upscales as the complexity of the ML application raises. In this case, the size of sample data was set according to problems of similar complexity, as shown in Parisi et al. [79], which employed about 5000 models. Increasing the complexity of the problem, the size of sample data increases, as for example shown by Parisi et al. [80], which adopted about 15000 models for training a graph neural network on a 2D truss-structure.

**Table 3**  
Hyperparameter tuning for each ML algorithm.

Model	Hyperparameter	Value
ANN	Neurons in 1st hidden layer	64
	Activation function of 1st hidden layer	ReLU
	Neurons in 2nd hidden layer	256
	Activation function of 2nd hidden layer	TanH
	Optimizer	Adam
	Epochs	600
	Loss function	MSE <sub>1</sub>
RFR	Number of trees in the Forrest	100
	Maximum number of levels in each decision tree	10
	Minimum number of samples required to be at a leaf node	6
SVR	C	0.2
	$\epsilon$	0.05
	Kernel	Rbf

### 3.5. Definition of ML surrogate models and discussion of the obtained results

For each generated model, the analyses defined in Section 2.2 were performed and results in terms of input ( $F_0$ ,  $E_c$ ,  $\Delta\epsilon^{(i,j)}$ ) and output ( $F_1$ ) parameters were stored. Hence, the training of the ML surrogate models (i.e., using all above-defined networks in Section 2.3) was performed through a machine equipped with a 11th Gen Intel® Core™ i9-11980HK @ 2.6 GHz (8 CPUs), 32 GBs DDR4 of RAM, and NVIDIA GeForce RTX 3080 GPU with 16 GBs. The sub-optimal values of hyperparameter

**Table 4**

Evaluation metrics results for training and test dataset of each ML surrogate model.

Set	Metric	ANN	RFR	SVR
Training	$R^2$	0.9999	0.9999	0.9945
	MAE	0.0016	0.0058	0.0216
	MSE <sub>1</sub>	4.12E-06	0.0088	6.5E-04
	RMSE	0.0019	0.0938	0.0255
Test	MSE <sub>2</sub>	6.13E-04	1.53E-03	-1.42E-03
	$R^2$	0.9999	0.9999	0.9845
	MAE	0.0017	0.0229	0.0213
	MSE <sub>1</sub>	4.57E-06	0.1090	6.5E-04
Test	RMSE	0.0021	0.3301	0.0257
	MSE <sub>2</sub>	6.44E-04	-4.58E-03	-1.00E-03

tuning employed in all models and obtained via grid search are reported in [Table 3](#), while training/test statistical metrics values are reported in [Table 4](#).

As observed, the obtained results for all ML models provide a good accuracy with optimal values of the evaluation metrics, which justify the use of the proposed models. In addition, although  $R^2$  values for each ML surrogate model overcame 0.99 in both training/test phases (see [Fig. 14](#)), some differences can be highlighted for the other statistical metrics in [Table 4](#). MAE values were lower than other models for the ANN (0.0016/0.0017), although the MAE obtained by RFR in the training phase (0.0058) was close to that by ANN. As discussed in [Section 2.4](#), MSE<sub>1</sub> and RMSE are the core statistical metrics. Given that a positive value of MSE<sub>2</sub> leads to underestimations of the output value, thus providing a conservative evaluation of  $F_1$ , ANN is the only ML Surrogate model to achieve this requirement (0.00061/0.00064), while negative values were obtained for RFR (0.0015/-0.0046) and SVR (-0.0014/-0.001). Still, ANN outperformed SVR and RFR by

considering RMSE (ANN: 0.0019/0.0021, RFR: 0.0938/0.03301, SVR: 0.0255/0.0257), and MSE<sub>1</sub> (ANN: 4.12E-06/4.57E-06, RFR: 0.0088/0.1090, SVR: 0.0006/0.0006). This result was expected given the ability of ANN to generalize problems. Using the RMSE to evaluate the capability of the model to predict prestressing losses (same unit measure), the obtained value by using ANN represent a lower bound in terms of prediction (i.e., the proposed model is able to predict low prestressing losses, up to 1.9 N).

After defining the three ML models, the choice of the surrogate was performed by checking the predictive capacity of each model toward the experimental tests. To this scope, all models were applied to predict the experimental values obtained in Phase 2, “low-damaged”, which was characterized by the removal of one bar over three, with a  $F_0$  equal to 330 kN and a  $F_1$  equal to 220 kN. The results are shown in [Table 5](#), where all models presented overall satisfying results. Nevertheless, the surrogate model made by ANN confirmed the best accuracy, having a percentage difference in terms of  $F_1$  of 0.3 %. It is worth noting that also RFR presented very good results, with a percentage difference of 0.4 % in terms of  $F_1$ .

It is worth noting that, although ANN presented high accuracy (see hyperparameter tuning shown in [Fig. 15](#)), there was no evidence of

**Table 5**

ML surrogate models  $F_1$  calculated values on Phase 2 “low-damaged” measurements.

ML Surrogate model	$F_1$ calculated [kN]	$F_1$ experimental [kN]	Difference [%]
ANN	219.43	220	0.3 %
RFR	219.13	220	0.4 %
SVR	209.78	220	4.6 %

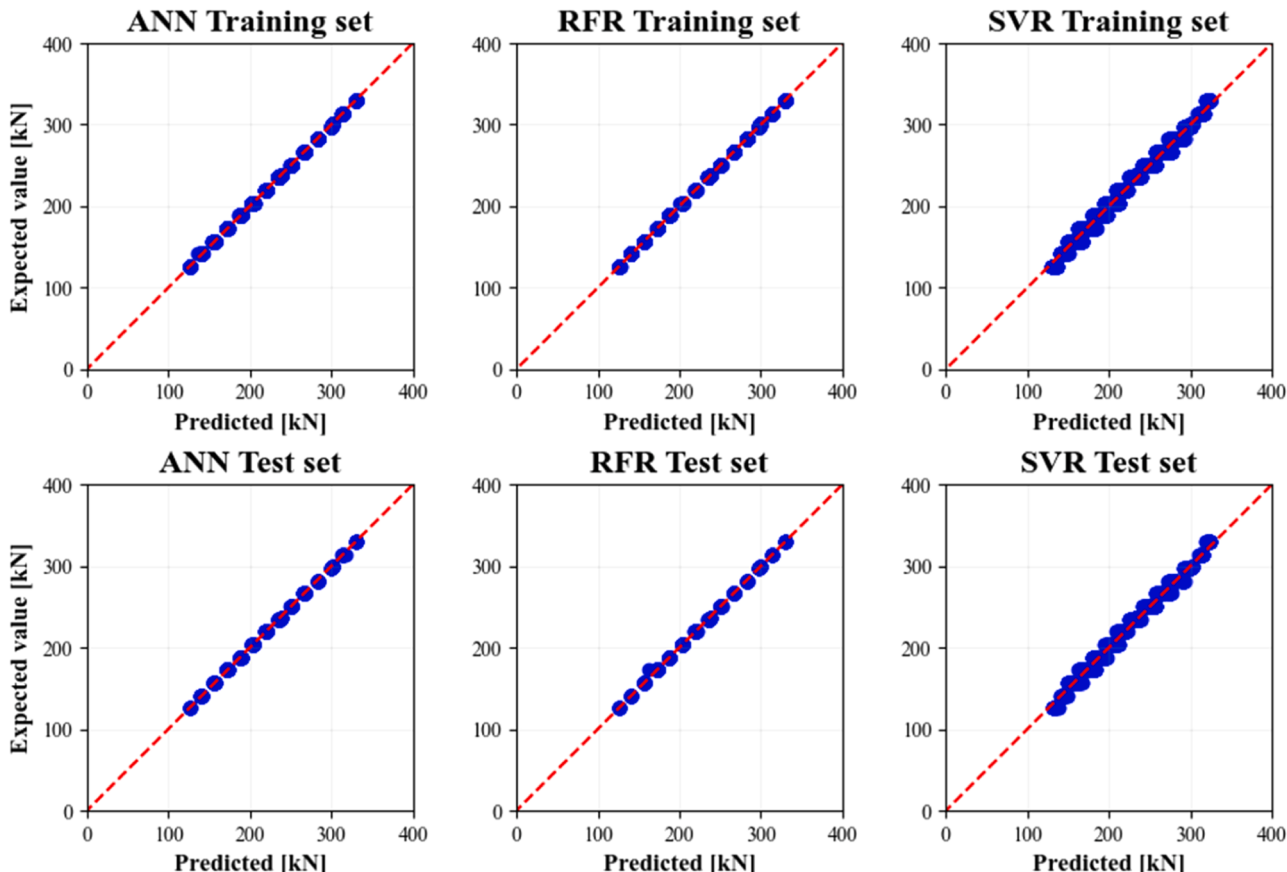


**Fig. 14.** ML surrogate models comparisons between predicted and expected value ( $F_1$ ) on training set (top row) and test set (bottom row). Red dashed line shows  $R^2$ .

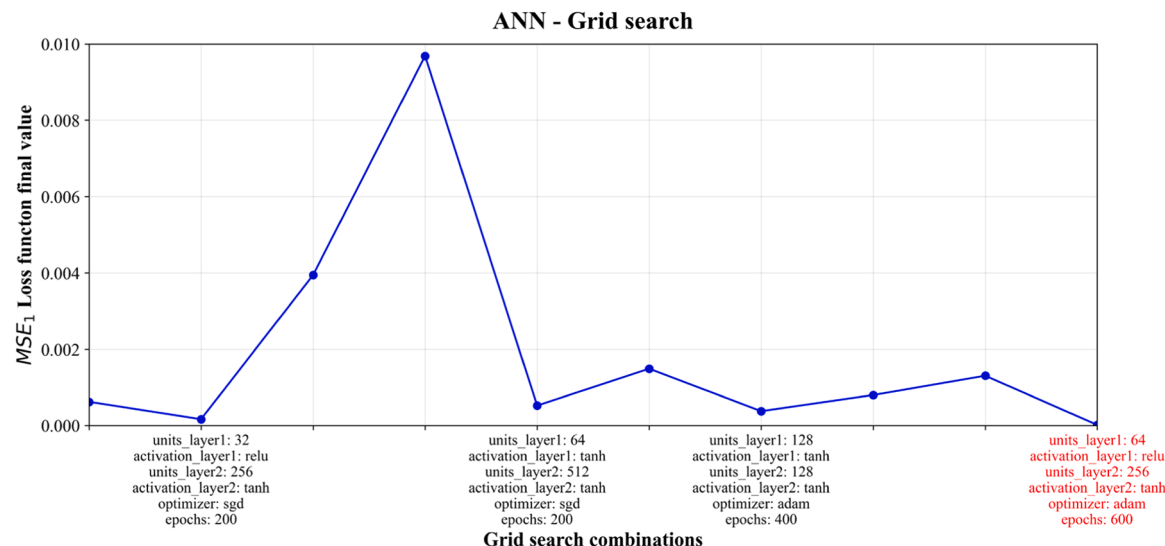


**Fig. 15.** Loss function ( $MSE_1$ ) values for some of the combinations of ANN hyperparameters used to select the best hyperparameter set (red one) reported in Table 3. In the abscissa, only few sets of hyperparameters (i.e., the more accurate) were reported, for the sake of clarity.

**Table 6**  
ANN K-fold cross-validation metrics results on training and validation sets.

Set	Metric	k-fold										Avg.	Std.
		1	2	3	4	5	6	7	8	9	10		
<b>Training</b>	$R^2$	0.9999	0.9999	0.9999	0.9999	0.9999	0.9999	0.9999	0.9999	0.9999	0.9999	0.9999	4E-05
	MAE	0.0025	0.0022	0.0015	0.0019	0.0013	0.0016	0.0022	0.0012	0.0008	0.0008	0.0016	5E-04
	$MSE_1$	8E-06	7E-06	3E-06	5E-06	3E-06	4E-06	7E-06	3E-06	1E-06	1E-06	4E-06	2E-06
	RMSE	0.0029	0.0025	0.0017	0.0022	0.0017	0.0019	0.0026	0.0017	0.0011	0.0011	0.0019	5E-04
<b>Validation</b>	$MSE_2$	2E-03	-2E-03	-3E-04	2E-03	-1E-03	-1E-03	2E-03	-7E-05	-1E-04	-1E-04	6E-04	1E-03
	$R^2$	0.9999	0.9999	0.9999	0.9999	0.9999	0.9999	0.9999	0.9999	0.9999	0.9999	0.9999	4E-05
	MAE	0.0026	0.0021	0.0016	0.0020	0.0014	0.0017	0.0022	0.0012	0.0009	0.0009	0.0017	5E-04
	$MSE_1$	8E-06	6E-06	5E-06	5E-06	3E-06	4E-06	7E-06	3E-06	1E-06	1E-06	4E-06	2E-06
	RMSE	0.0029	0.0025	0.0023	0.0023	0.0018	0.0021	0.0026	0.0018	0.0012	0.0014	0.0021	5E-04
	$MSE_2$	3E-03	-2E-03	-3E-04	-2E-03	1E-03	-1E-03	2E-03	-2E-04	-2E-04	-1E-04	6E-04	1E-03

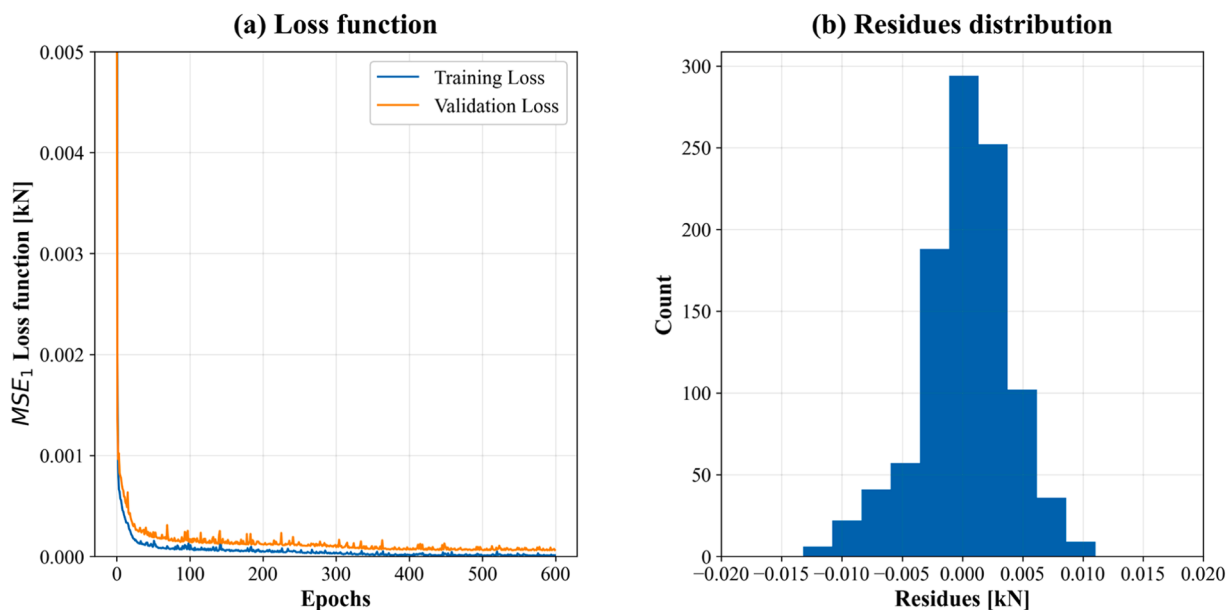


**Fig. 16.** (a) ANN loss function values, (b) Residues distribution of test data.

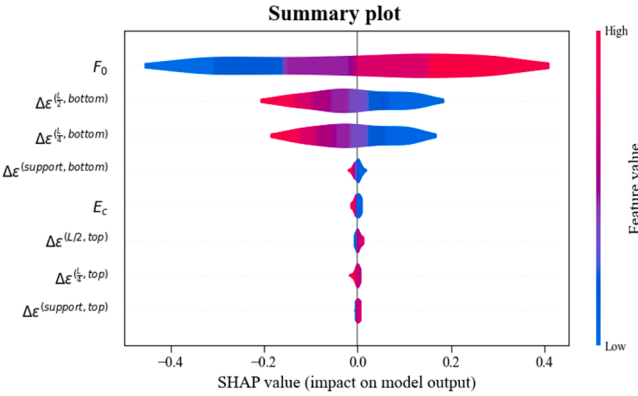


Fig. 17. SHAP results for  $F_1$  output feature.

overfitting problems. In fact, as performed in several existing papers (e.g., [81]), by assessing the performance of the proposed ML model to the training and test data, properly split, the overfitting problem can occur if the model performs significantly better on the training set than the test set. To check this aspect, two main controls were performed: (a) definition of k-fold cross-validation to evaluate the model performance; and (b) comparison of the loss function between training and test datasets. Regarding the k-fold cross-validation, a 10 k-fold subdivision was considered and statistical metrics results for each fold are reported in Table 6, together with the related mean and standard deviation (mean values for training set are the same reported in Table 4 for ANN). Regarding the loss function, the  $MSE_1$  metric was used, and the results are shown in Fig. 16(a) for ANN. Loss function for training and test datasets were similar, confirming the absence of overfitting for the proposed surrogate model. Still, Fig. 16(b) reports the residues for the test dataset, to denote a normal-like distribution of this quantity, which suggests that errors are random and not correlated.

Finally, an eXplainability approach was used on the proposed ML surrogate model to assess the influence of each considered parameter on the simulated prestressing loss. It is worth reminding that this step is important because it can provide some insights about the most influent concrete strain values on the results, which in turn can suggest how to design sensors-based systems aimed at monitoring the prestressing losses. With this goal in mind, the SHAP method was employed through SHAP Python package, and the results are shown in Fig. 17 and Fig. 18. In particular, Fig. 17 reports the summary plot with input features in ordinate, ranked on the base of their influence on the results, and in abscissa the value of the impact of each feature on the predictive capacity of the model. A red color indicates increasing output value while a blue color denotes decreasing output value. As expected, the most influential value is  $F_0$ . The second and the third influent parameters are the strain measures at the bottom fiber of the  $L/2$  section,  $\Delta\epsilon^{(L/2, bottom)}$ , and bottom fiber of  $L/4$  section,  $\Delta\epsilon^{(L/4, bottom)}$ . The density of the red color changes when  $F_0$  increases, from which it can be deduced that  $F_1$  increases as  $F_0$  increases. On the contrary, an increment in  $\Delta\epsilon^{(L/2, bottom)}$  and  $\Delta\epsilon^{(L/4, bottom)}$  corresponds to an  $F_1$  decrease, and this is an important achievement because the proposed model allows characterizing the relation between strain in some specific points and loss of prestressing force.

Fig. 18 reports the SHAP dependence plot, aiming at interpreting the effects of each feature and their interactions within the model. The plots provide a bi-dimensional view showing the relationship between the value of a feature (abscissa) and its SHAP value (ordinate), reporting then the contribution of each feature to the predictions. The obtained magnitude of values on the ordinates for each input parameter confirms the outcomes in Fig. 17, while abscissa values are reported in the normalized scale used for ANN training. A negative trend in the graphs (e.g., Fig. 18(d), (f) and (h)) implies that as the input value increases the output value,  $F_1$ , decreases. Conversely a positive trend in the graph (e.g.,

Fig. 18(b)) means that as the input value increases the output value,  $F_1$ , increases. Hence, as  $\Delta\epsilon^{(L/2, bottom)}$ ,  $\Delta\epsilon^{(L/4, bottom)}$  and  $\Delta\epsilon^{(support, bottom)}$  increase,  $F_1$  decreases. On the other hand, as  $F_0$  increases,  $F_1$  tends to increase. The input variable that may have an interaction effect with the plotted feature is represented in the colormap. If an interaction effect is present between two features, a distinct vertical pattern of coloring is shown. Fig. 18(b) shows the impact on  $F_0$  related SHAP value given the variation of  $\Delta\epsilon^{(L/4, bottom)}$ . For  $F_0$  values above 0.5, a reduction in  $\Delta\epsilon^{(L/4, bottom)}$  increases the SHAP value of  $F_0$ , while for  $F_0$  values below 0.5, an increase in  $\Delta\epsilon^{(L/4, bottom)}$  value decreases the SHAP value of  $F_0$ . This is physically true because lower strain increments suggest a higher  $F_1$  value, and thus a lower prestressing force reduction. Conversely, Fig. 18(f) and (h) show that for input feature values  $\Delta\epsilon^{(L/2, bottom)}$  and  $\Delta\epsilon^{(L/4, bottom)}$  above 0.5, a decrement in  $E_c$  reduces the SHAP value of the input feature. For the same features, while their values are below 0.5, an increment in  $E_c$  increases the SHAP value. The mathematical relation proposed by the ANN is simple to capture, because higher values of  $E_c$  correspond to lower strain increments, and thus a lower prestressing force reduction.

show that for input feature values  $\Delta\epsilon^{(L/2, bottom)}$  and  $\Delta\epsilon^{(L/4, bottom)}$  above 0.5, a decrement in  $E_c$  reduces the SHAP value of the input feature. For the same features, while their values are below 0.5, an increment in  $E_c$  increases the SHAP value. The mathematical relation proposed by the ANN is simple to capture, because higher values of  $E_c$  correspond to lower strain increments, and thus a lower prestressing force reduction.

#### 4. Conclusions

The paper proposed a framework to define a Machine Learning (ML)-based surrogate model able to predict the prestressing losses of unbonded strands in prestressed concrete (PSC) box-girder bridges. The developed surrogate model aims to support a reliable structural assessment and monitoring of PSC box-girder bridges. The structural safety management of these structures involves the characterization of the health state of internal unbonded tendons (which are often inaccessible), the continuous record of the effective prestressing force reduction over time, and the design of an effective structural health monitoring (SHM) system. To these scopes, the proposed framework is based on the results obtained by experimental tests on a scaled PSC box-girder bridge, made in the ICITECH laboratory of the *Universitat Politècnica de València*. The scaled box-girder specimen, instrumented with linear variable displacement transducer sensors and strain gauges, was tested under a Four-point bending test on different phases, accounting for an undamaged phase (i.e., Phase 1) and three progressive damaged phases (i.e., Phases 2, 3, 4). From the obtained results, a simple but effective nonlinear Finite Element (FE) model was developed and validated. In particular, both undamaged and damaged phases were assessed for the calibration, obtaining average percentage differences equal to 1 % and 2 % for displacement and stress values, respectively. Using the defined modelling approach and including variability for geometrical and mechanical properties, i.e., the elastic modulus of concrete ( $E_c$ ) and prestressing force at the “initial state” ( $F_0$ ), a sample dataset was generated by defining 5031 FE models. Using the above data, three ML algorithms were trained (Artificial Neural Network, ANN, Random Forest Regressor, and Support Vector Regression) to relate the prestressing losses (i.e.,  $F_1$ ) to the input variables (i.e.,  $E_c$ ,  $F_0$ , and the strain variation in different sections,  $\Delta\epsilon^{(l, j)}$ ). By using adequate evaluation metrics, the prediction provided by ANN resulted the most accurate, revealing the best algorithm to define the ML surrogate model. In addition, input variables were ranked through an eXplainability approach to evaluate their impact on the target variable prediction. The results can be summarized as follows:

- A correct definition of  $F_0$  is required in the “initial state”, that is the time of investigation.

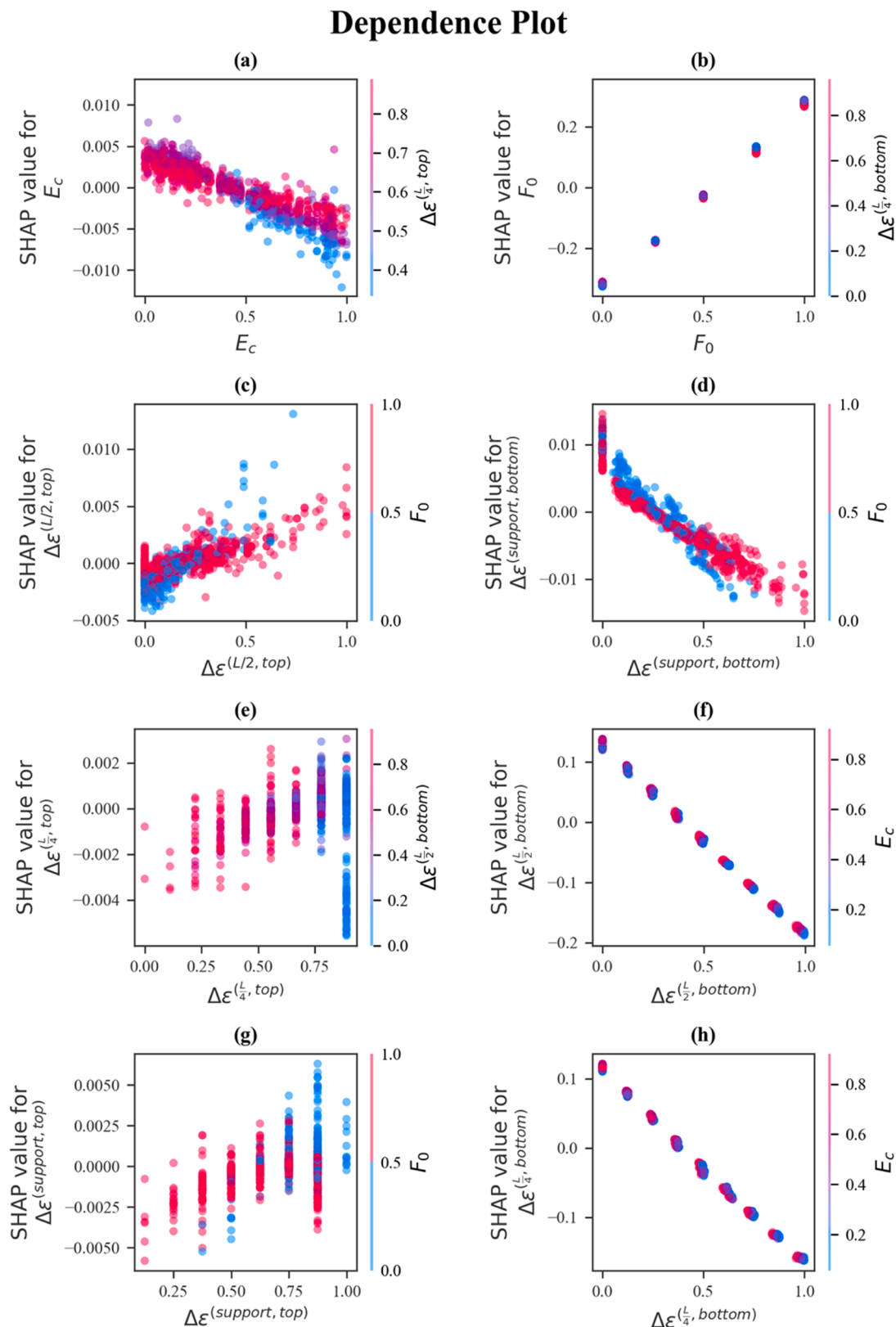


**Fig. 18.** Dependence plot, on abscissa input feature, on ordinate its SHAP value on output feature and colormap shows the values of the input variable that may have an interaction effect with the plotted input feature.

- The value of  $E_c$  presents a low impact on the overall results, even though its role is fundamental in the definition of  $\Delta\epsilon^{(i,j)}$ .
- An effective sensors-based SHM system, aimed at assessing pre-stressing losses, can be employed for this typology of bridge, by placing strain gauges at the bottom fibers of  $L/2$  and  $L/4$  sections ( $L$  is the length of the beam).

The results presented in this study suggest that the proposed ML surrogate model allows overcoming the limitations characterizing the traditional non-destructive methods, which require periodic and expensive onsite tests. In fact, to derive the current prestressing losses, it is necessary to characterize the values of  $F_0$  and  $E_c$  in the “initial state” and ensure continuous strain monitoring in the specific points above indicated. One limitation of the study is represented by the scaled model, which presents some simplifications in its manufacturing. In fact, the scaled bridge presents a beam section designed according to the indication by Agarwal et al. [82], but other quantities were not scaled (as for example made by Losanno et al. [20]). Moreover, the realization of other specimens with different geometrical and mechanical feature could improve the dataset at the base of the proposed ML model, which at the current state was numerically generated. In addition, those data could be used also for elaborating different type of predicting models, such as by employing more classical probabilistic-based approaches.

#### Author statement

I hereby confirm that all authors named in the manuscript are aware of the submission and have agreed for the paper to be submitted to *Engineering Structures*.

#### CRediT authorship contribution statement

**Giuseppina Uva:** Writing – review & editing, Supervision, Resources, Project administration. **Andrea Nettis:** Writing – review & editing, Methodology, Conceptualization. **Jose Miguel Adam:** Writing – review & editing, Supervision, Resources, Project administration. **Sergio Ruggieri:** Writing – original draft, Supervision, Methodology, Formal analysis, Conceptualization. **Manuel Buitrago:** Writing – review & editing, Methodology, Investigation. **Mirko Calò:** Writing – original draft, Validation, Software, Methodology, Investigation, Formal analysis, Data curation, Conceptualization.

#### Declaration of Competing Interest

The authors declare the following financial interests/personal relationships which may be considered as potential competing interests: Mirko Calò acknowledges funding by Italian Ministry of University and Research, within the project ‘PON-Ricerca e Innovazione-2014–2020, CUP Code (D.M. 10/08/2021, n. 1061): D95F21002340006. Sergio Ruggieri acknowledges funding by Italian Ministry of University and Research, within the project ‘PON-Ricerca e Innovazione-2014–2020, CUP Code (D.M. 10/08/2021, n. 1062): D95F21002140006. Manuel Buitrago declares funding received under the postdoctoral Grant IJC2020-042642-I funded by MCIN/AEI/ 10.13039/501100011033 and by the “European Union NextGenerationEU/PRTR”. Andrea Nettis and Giuseppina Uva acknowledge the Sustainable Mobility National Research Center (MOST) and received funding from the European Union Next-GenerationEU (PIANO NAZIONALE DI RIPRESA E RESILIENZA (PNRR) – MISSIONE 4 COMPONENTE 2, INVESTIMENTO 1.4 – D.D. 1033 17/06/2022, CN00000023) - SPOKE 7 “CCAM, Connected Networks and Smart Infrastructure” - WP4 (CUP D93C22000410001). Finally, Jose M. Adam and all co-authors acknowledge the invaluable cooperation of the Calsens Spin-off company during the execution of the test of the scaled bridge.

#### Acknowledgments

Mirko Calò acknowledges funding by Italian Ministry of University and Research, within the project ‘PON-Ricerca e Innovazione-2014–2020, CUP Code (D.M. 10/08/2021, n. 1061): D95F21002340006. Sergio Ruggieri acknowledges funding by Italian Ministry of University and Research, within the project ‘PON-Ricerca e Innovazione-2014–2020, CUP Code (D.M. 10/08/2021, n. 1062): D95F21002140006. Manuel Buitrago declares funding received under the postdoctoral Grant IJC2020-042642-I funded by MCIN/AEI/ 10.13039/501100011033 and by the “European Union NextGenerationEU/PRTR”. Andrea Nettis and Giuseppina Uva acknowledge the Sustainable Mobility National Research Center (MOST) and received funding from the European Union Next-GenerationEU (PIANO NAZIONALE DI RIPRESA E RESILIENZA (PNRR) – MISSIONE 4 COMPONENTE 2, INVESTIMENTO 1.4 – D.D. 1033 17/06/2022, CN00000023) - SPOKE 7 “CCAM, Connected Networks and Smart Infrastructure” - WP4 (CUP D93C22000410001). Finally, Jose M. Adam and all co-authors acknowledge the invaluable cooperation of the Calsens Spin-off company during the execution of the test of the scaled bridge.

#### Appendix: Nomenclature

- [A] Value matrix of the neuron layer in the ANN model.
- [B] Bias vector of the hidden layer in the ANN model.
- [X] Input vector of the ANN model.
- [W<sub>1</sub>] Weight matrix associated to [X].
- [W<sub>2</sub>] Weight matrix associated to [A].
- $a_u$  Output value of the  $u$ th neuron in the hidden layer of the ANN model.
- ANN Artificial Neural Network.
- $b_u$  Bias associated with the activation of the  $u^{th}$  neuron of the ANN model.
- $C$  Positive constant in the SVR model.
- DT Decision Tree.
- $E_c$  Elastic modulus of concrete at the time of sensor installation.
- $f(x, \alpha)$  Regression function of the SVR model.
- $F$  Set of function of the SVR model.
- $F_0$  Initial prestressing force at the time of sensor installation.
- $F_1$  Residual prestressing force.
- $F_k$  Generic initial prestressing force at the time of sensor installation.
- FBG Fiber Bragg gratings sensor.
- FE Finite Element model.

- $h_{nl(x)}$  Individual prediction of a DT.
- $\hat{h}_{RF}^{n_t}$  Prediction of the RFR.
- $L$  Length of the beam specimen.
- $MAE$  Mean Absolute Error.
- $ML$  Machine Learning.
- $MSE_1$  Mean Squared Error.
- $MSE_2$  Mean Signed Error.
- $n$  Number of neurons in the input layer of the ANN.
- $n_t$  Number of trees in the RFR.
- $N$  Sample data in SHAP method.
- $o$  Input feature evaluated in SHAP method.
- $p$  Number of data points.
- $r$  Generic record of  $N$ .
- $R^2$  Coefficient of determination.
- $R_d$  Distinct and non overlapping region.
- $PSC$  Prestressed reinforced concrete.
- $RFR$  Random Forrest Regressor.
- $RMSE$  Root Mean Squared Error.
- $S$  Subset of  $N$  which do not include  $o$ .
- $SHAP$  SHapley Additive exPlanation.
- $T$  Training data.
- $u$  Number of distinct and nonoverlapping regions.
- $v$  Natural number between 1 and  $n$ .
- $V$  Vapnik's  $\epsilon$ -insensitive loss function.
- $w_v$  Weight associated to  $x_v$ .
- $x_v$  Element of the column vector  $[X]$ .
- $x_c$  Input element of the set of training data  $z$ .
- $y$  Generic prediction of ML model.
- $y_c$  Output value in  $z$ .
- $y_m$  Experimental value.
- $\hat{y}_m$  Predicted value.
- $z$  Subset of  $T$  for the SVR model.
- $Z$  Set of parameters of the SVR model.
- $\beta$  Optimal separating hyperplane in the SVR model.
- $\gamma_o$  SHAP value.
- $\delta$  ML trained model.
- $\Delta\epsilon_{model}^{(i,j)}$  Strain increment at  $j^{\text{th}}$  fiber of the  $i^{\text{th}}$  section given by the difference between  $\epsilon_{(b)}^{(i,j)}$  and  $\epsilon_{(a)}^{(i,j)}$ .
- $\Delta\epsilon_{RF}^{(i,j)}$  Strain increment at  $j^{\text{th}}$  fiber of the  $i^{\text{th}}$  section under a generic  $F_k$  value.
- $\Delta\epsilon^{(i,j)}$  Strain increment at  $j^{\text{th}}$  fiber of the  $i^{\text{th}}$  section due to prestressing loss.
- $\epsilon$  Residual threshold in the SVR model.
- $\epsilon_{(a)^{(i,j)}}$  Absolute numerical strain values at step (a).
- $\epsilon_{(b)^{(i,j)}}$  Absolute numerical strain values at step (b).
- $\mu_e$  Average of experimental values.
- $\xi_c, \xi_c^*$  Slack variables in the SVR model.
- $\varphi$  Nonlinear function of the SVR model.
- $\psi$  Activation function of the ANN model.

## Data availability

Data will be made available on request.

## References

- [1] Calvi GM, Moratti M, O'Reilly GJ, Scattarreggia N, Monteiro R, Malomo D, et al. Once upon a time in Italy: the tale of the Morandi Bridge. *Struct Eng Int* 2019;29(2):198–217. <https://doi.org/10.1080/10168664.2018.1558033>.
- [2] Farneti E, Cavalagli N, Costantini M, Trillo F, Minati F, Venanzi I, et al. A method for structural monitoring of multispan bridges using satellite InSAR data with uncertainty quantification and its pre-collapse application to the Albiano-Magra Bridge in Italy. *Struct Health Monit* 2022;22(1):353–71. <https://doi.org/10.1177/14759217221083609>.
- [3] Ministero delle Infrastrutture e dei Trasporti. Linee Guida per la Classificazione e Gestione del Rischio, la Valutazione della Sicurezza ed il Monitoraggio dei Ponti Esistenti, Italy, 2020.
- [4] Adam JM, Makond N, Riveiro B, Buitrago M. Risks of bridge collapses are real and set to rise — here's why. *Nature* 2024;629:1001–3. <https://doi.org/10.1038/d41586-024-01522-6>.
- [5] W. Salvatore , G. Uva , I. Venanzi , C. Mazzotti , M. Morici , A. Natali , , et al. et al. Application of Italian Guidelines for structural-foundational and seismic risk classification of bridges: the Fabre experience on a large bridge inventory. Proceedings of II Fabre Conference – Existing bridges, viaducts and tunnels: research, innovation and applications, 2024.
- [6] Tyson D. The history of prestressed concrete: 1888 to 1963. *K-State Electronic Theses, Dissertations, and Reports: 2004*. KANSAS STATE UNIVERSITY. USA: Lawrence; 2009.
- [7] Naito C, Sause R, Hodgson I, Pessiki S, Macioce T. Forensic estimation of a noncomposite adjacent precast prestressed concrete box beam bridge. *J Bridge Eng* 2010;15(4):408–18. [https://doi.org/10.1061/\(ASCE\)BE.1943-5592.0000110](https://doi.org/10.1061/(ASCE)BE.1943-5592.0000110).
- [8] Corven J. Post-Tensioned, Box Girder Design Manual. Federal Highway Administration; 2015. <https://www.fhwa.dot.gov/bridge/concrete/hif15016.pdf>.
- [9] Chávez AA, Gonzalez-Libreros J, Wang C, Capacci L, Biondini F, Elfgrén L, et al. Assessment of residual prestress in existing concrete bridges: the Kalix bridge. *Eng Struct* 2024;311. <https://doi.org/10.1016/j.engstruct.2024.118194>.
- [10] Sconocchia GG, Mariani F, Ierimonti L, Meoni A, Venanzi I, Ubertino F. Insights into structural assessment and long-term effects of post-tensioned multispan concrete box girder bridge with vertically prestressed internal joints. *Structures* 2024;63. <https://doi.org/10.1016/j.istruc.2024.106396>.

- [11] Kim D, Shim C-S. An experimental study on the deterioration behaviour of external tendons due to corrosion. KSCE J Civ Eng 2023;27:5319–28. <https://doi.org/10.1007/s12205-023-0316-5>.
- [12] Bazant ZP, Jirásek M. Paradigms of application, phenomena affecting creep deformations, and comparisons to measurements on structures. Creep and hygrothermal effects in concrete structures. Solid Mech Appl 2019;225. [https://doi.org/10.1007/978-94-024-1138-6\\_7](https://doi.org/10.1007/978-94-024-1138-6_7).
- [13] Yang M, Gang J, Yang X. Refined calculation of time-dependent prestress losses in prestressed concrete girders. Struct Infrastruct Eng 2020;16(10):1430–46. <https://doi.org/10.1080/15732479.2020.1712438>.
- [14] Huang H, Huang S-S, Pilakoutas K. Modeling for assessment of long-term behavior of prestressed concrete box-girder bridges. J Bridge Eng 2018;23(3). [https://doi.org/10.1061/\(ASCE\)BE.1943-5592.0001210](https://doi.org/10.1061/(ASCE)BE.1943-5592.0001210).
- [15] Ministero delle Infrastrutture e dei Trasporti. Aggiornamento delle <<Norme tecniche per le costruzioni>>, Italy, 2018.
- [16] ACI Committee 318. Building Code Requirements for Structural Concrete and Commentary (ACI 318-19), 2022.
- [17] Tu B, Dong Y, Fang Z. Time-dependent reliability and redundancy of corroded prestressed concrete bridges at material, component, and system levels. J Bridge Eng 2019;24(9). [https://doi.org/10.1061/\(ASCE\)BE.1943-5592.0001461](https://doi.org/10.1061/(ASCE)BE.1943-5592.0001461).
- [18] Bazant Z, Yu Q. Relaxation of prestressing steel at varying strain and temperature: viscoplastic constitutive relation. J Eng Mech 2013;139(7):814–23. [https://doi.org/10.1061/\(ASCE\)EM.1943-7889.0000533](https://doi.org/10.1061/(ASCE)EM.1943-7889.0000533).
- [19] Losanno D, Galano S, Parisi F. Influence of strand rupture on flexural behavior of reduced-scale prestressed concrete bridge girders with different prestressing levels. Eng Struct 2024;301:117358. <https://doi.org/10.1016/j.engstruct.2023.117358>.
- [20] Losanno D, Galano S, Parisi F, Pecce MR, Cosenza E. Experimental investigation on nonlinear flexural behavior of post-tensioned concrete bridge girders with different grouting conditions and prestress levels. J Bridge Eng 2023;29(3). <https://doi.org/10.1061/JBENF2.BEENG-6466>.
- [21] Zia P, Kent HPreston, Scott NL, Workman EB. Estimating prestress losses. Concr Int 1979;1(6).
- [22] Franceschini L, Vecchi F, Belletti B, Andrade C, Peiretti H-C. Analytical method for the evaluation of the residual service life of prestressed concrete beams subjected to corrosion deterioration. Struct Concr 2023;23(1):121–37. <https://doi.org/10.1002/suco.202100245>.
- [23] Nettis A, Nettis A, Ruggieri S, Uva G. Corrosion-induced fragility of existing prestressed concrete girder bridges under traffic loads. Eng Struct 2024;314. <https://doi.org/10.1016/j.engstruct.2024.118302>.
- [24] (<https://www.transportes.gob.es/el-ministerio/sala-de-prensa/noticias/mar-15-112022-1613>).
- [25] He Z-Q, Li Y, Xu T, Liu Z, Ma ZJ. Crack-based serviceability assessment of post-tensioned segmental concrete box-girder bridges. Structures 2021;30:1097–108. <https://doi.org/10.1016/j.istruc.2021.01.062>.
- [26] Sousa H, Bento J, Figueiras J. Assessment and management of concrete bridges supported by monitoring data-based finite-element modeling. J Bridge Eng 2014;19(6). [https://doi.org/10.1061/\(ASCE\)BE.1943-5592.0000604](https://doi.org/10.1061/(ASCE)BE.1943-5592.0000604).
- [27] Comisú C-C, Taranu N, Boaca G, Scutaru M-C. Structural health monitoring system of bridges. Procedia Eng 2017;199:2054–9. <https://doi.org/10.1016/j.proeng.2017.09.472>.
- [28] He Z, Li W, Salehi H, Zhang H, Zhou H, Jiao P. Integrated structural health monitoring in bridge engineering. Autom Constr 2022;136. <https://doi.org/10.1016/j.autcon.2022.104168>.
- [29] Sousa H, Félix C, Bento J, Figueiras J. Design and implementation of a monitoring system applied to a long-span prestressed concrete bridge. Struct Concr 2011;12(2):82–93. <https://doi.org/10.1002/suco.201000014>.
- [30] Dall'Asta A, Dezi L. Discussion on “Prestress force effect on vibration frequency of concrete bridges”. J Struct Eng 1996;122(4). [https://doi.org/10.1061/\(ASCE\)0733-9445\(1996\)122:4\(459\)](https://doi.org/10.1061/(ASCE)0733-9445(1996)122:4(459)).
- [31] Hamed E, Frosting Y. Natural frequencies of bonded and unbonded prestressed beams—prestress force effects. J Sound Vib 2006;295(1-2):28–39. <https://doi.org/10.1016/j.jsv.2005.11.032>.
- [32] Abraham MA, Park S, Stubbs N. Loss of prestress prediction based on nondestructive damage location algorithms. Proc Smart Struct Mater: Smart Syst Bridges Struct Highw 1995;2446. <https://doi.org/10.1117/12.207717>.
- [33] Limongelli MP, Siegert D, Merliot E, Waeytens J, Bourquin F, Vidal R, et al. Damage detection in a post tensioned concrete beam – experimental investigation. Eng Struct 2016;128:15–25. <https://doi.org/10.1016/j.engstruct.2016.09.017>.
- [34] Bonopera M, Chang KC, Chen CC, Sung YC, Tullini N. Prestress force effect on fundamental frequency and deflection shape of PCI beams. Struct Eng Mech 2018;67(3):255–65. <https://doi.org/10.12989/seam.2018.67.3.255>.
- [35] De Angelis A, Losanno D, Parisi F, Pecce MR. Identification of modal parameters of scaled bridge PC beams by OMA dynamic tests. J Bridge Eng 2024;29(8). <https://doi.org/10.1061/JBENF2.BEENG-6763>.
- [36] Park G, Sohn H, Farrar CR, Inman DJ. Overview of piezoelectric impedance-based health monitoring and path forward. Shock Vib Dig 2023;35(6):451–63. <https://doi.org/10.1177/05831024030356001>.
- [37] Rabelo D, Finzi Neto RM, Steffen V. Impedance-based structural health monitoring incorporating compensation of temperature variation effects. 23rd ABCM Int Congr Mech Eng 2015. <https://doi.org/10.20906/CPS/COB-2015-1903>.
- [38] Huynh T-C, Kim J-T. Impedance-based cable force monitoring in tendon-anchorages using portable PZT-interface technique. Math Probl Eng 2014. <https://doi.org/10.1155/2014/784731>.
- [39] Kim ST, Park Y, Park SY, Cho J-R. A sensor-type PC strand with an embedded fbg sensor for monitoring prestress forces. Sensors 2015;15(1):1060–70. <https://doi.org/10.3390/s150101060>.
- [40] McKeeman I, Fusiek G, Perry M, Johnston M, Saafi M, Niewczas P, et al. First-time demonstration of measuring concrete prestress levels with metal packaged fibre optic sensors. Smart Mater Struct 2015;25(9). <https://doi.org/10.1088/0964-1726/25/9/095051>.
- [41] Cheng S-Z, Wu G, Xing T, Feng D-C. Prestressing force monitoring method for a box girder through distributed long-gauge FGB sensors. Smart Mater Struct 2018;27. <https://doi.org/10.1088/1361-665X/aa9bbe>.
- [42] Liu C, Teng J, Wu N. A wireless strain sensor network for structural health monitoring. Shock Vib 2015. <https://doi.org/10.1155/2015/740471>.
- [43] Jo H, Park J-W, Spencer BF, Jung H-J. Development of high-sensitivity wireless strain sensor for structural health monitoring. Smart Struct Syst 2013;11(5):477–96. <https://doi.org/10.12989/ss.2013.11.5.477>.
- [44] H. Abdel-Jaber. Comprehensive strain-based methods for monitoring prestressed concrete beam-like elements. Ph.D. Thesis: Princeton University. (2017).
- [45] Bonopera M, Chang K-C. Novel method for identifying residual prestress force in simply supported concrete girder-bridges. Adv Struct Eng 2021;24(14):3238–51. <https://doi.org/10.1177/13694332211022067>.
- [46] Abdel-Jaber H, Glisic B. Monitoring of prestressing forces in prestressed concrete structures—an overview. Struct Control Health Monit 2019;26. <https://doi.org/10.1002/stc.237>.
- [47] Xiong C, Zayed T, Abdelkader EM. A novel YOLOv8-GAM-Wise-IoU model for automated detection of bridge surface cracks. Constr Build Mater 2021;414. <https://doi.org/10.1016/j.conbuildmat.2024.135025>.
- [48] Wan H, Gao L, Yuan Z, Qu H, Sun Q, Cheng H, et al. A novel transformer model for surface damage detection and cognition of concrete bridges. Expert Syst Appl 2023;213(B)). <https://doi.org/10.1016/j.eswa.2022.119019>.
- [49] Mei Q, Güll M. Indirect health monitoring of bridges using Mel-frequency cepstral coefficients and principal component analysis. Mech Syst Signal Process 2018;119:523–46. <https://doi.org/10.1016/j.jmssp.2018.10.006>.
- [50] Sakiyama F, Verissimo GS, Garrech H. Quantifying the extent of local damage of a 60-year-old prestressed concrete bridge: a hybrid SHM approach. Struct Health Monit 2023;22(1):496–517. <https://doi.org/10.1177/14759217221079295>.
- [51] Svendsen BT, Frøseth GT, Øiseth O, Rønningst A. A data-based structural health monitoring approach for damage detection in steel bridges using experimental data. J Civ Struct Health Monit 2022;12:101–15. <https://doi.org/10.1007/s13349-021-00530-8>.
- [52] Chen S, Duffield C, Miramini S, Raja BNK, Zhang L. Life-cycle modelling of concrete cracking and reinforcement corrosion in concrete bridges: A case study. Eng Struct 2021;237. <https://doi.org/10.1016/j.engstruct.2021.112143>.
- [53] Mangalathu S, Heo G, Jeon J-S. Artificial neural network based multi-dimensional fragility development of skewed concrete bridge classes. Eng Struct 2018;162. <https://doi.org/10.1016/j.engstruct.2018.01.053>.
- [54] Mo R, Chen L, Xing Z, Ye X, Xiong C, Liu C, et al. Bridge seismic fragility model based on support vector machine and relevance vector machine. Structures 2023;52:768–78. <https://doi.org/10.1016/j.istruc.2023.03.179>.
- [55] Opabode EA, Mangalathu S. Seismic fragility assessment of bridges with as-built and retrofitted splice-deficient columns. Bull Earthq Eng 2023;21:583–603. <https://doi.org/10.1007/s10518-022-01521-w>.
- [56] Soleimani F, Liu X. Artificial neural network application in predicting probabilistic seismic demands of bridge components. Earthq Engng Struct Dyn 2022;51(3):612–29. <https://doi.org/10.1002/eqe.3582>.
- [57] Dang N-L, Phan N-T-V, Ho D-D, Kim J-T, Huynh T-C. A hybrid method for strand looseness identification in post-tensioned system using FEM and ANN. J Civ Struct Health Monit 2023;13:1287–311. <https://doi.org/10.1007/s13349-023-00704-6>.
- [58] Marinello G, Pastore T, Asprone D, Cosenza E. Layout-aware extreme learning machine to detect tendon malfunctions in prestressed concrete bridges using stress data. Autom Constr 2021;132. <https://doi.org/10.1016/j.autcon.2021.103976>.
- [59] Kim J, Park S. Field applicability of a machine learning-based tensile force estimation for pre-stressed concrete bridges using an embedded elasto-magnetic sensor. Struct Health Monit 2020;19(1):281–92. <https://doi.org/10.1177/1475921719842340>.
- [60] Nguyen T-T, Phan TTV, Ho D-D, Pradhan AMS, Huynh T-C. Deep learning-based autonomous damage-sensitive feature extraction for impedance-based prestress monitoring. Eng Struct 2022;259. <https://doi.org/10.1016/j.engstruct.2022.114172>.
- [61] M.L. Scott, S.-I. Lee. A Unified Approach to Interpreting Model Predictions. *Proceedings of the 31st Annual Conference on Neural Information Processing Systems, Long Beach, CA*. (2017). <https://doi.org/10.48550/arXiv.1705.07874>.
- [62] Hou P, Yang C, Yang J, Pan Y. Investigation on mechanical performance of prestressed concrete box-girder bridge strengthened using composite trusses with different shapes. Struct Concr 2024;25(3):1620–36. <https://doi.org/10.1002/suco.202300183>.
- [63] Pérez-Sala JC, Ruiz-Teran AM. Numerical analysis of precast concrete segmental bridge decks. Eng Struct 2023;275(A)). <https://doi.org/10.1016/J.ENGSTRUCT.2022.115277>.
- [64] Noble D, Nogal M, O'Connor A, Pakrashi V. The effect of prestress force magnitude and eccentricity on the natural bending frequencies of uncracked prestressed concrete beams. J Sound Vib 2016;365:22–44. <https://doi.org/10.1016/j.jsv.2015.11.047>.
- [65] Eurocode 2, EN 1992-1-1:2004, Eurocode 2: Design of concrete structures - Part 1-1: General rules and rules for buildings, 2004.
- [66] Nettis A, Raffaele D, Uva G. Seismic risk-informed prioritisation of multi-span RC girder bridges considering knowledge-based uncertainty. Bull Earthq Eng 2024;22:693–729. <https://doi.org/10.1007/s10518-023-01783-y>.

- [67] Bagge N, Nilimaa J, Elfgren L. In-situ methods to determine residual prestress forces in concrete bridges. Eng Struct 2017;135:41–52. <https://doi.org/10.1016/j.engstruct.2016.12.059>.
- [68] Wang Y, Zheng Z, Ji D, Pan X, Tian A. Machine learning-driven probabilistic seismic demand model with multiple intensity measures and applicability in seismic fragility analysis for nuclear power plants. Soil Dyn Earthq Eng 2023;171. <https://doi.org/10.1016/j.soildyn.2023.107966>.
- [69] Breiman L. Random forests. Mach Learn 2001;45:5–32. <https://doi.org/10.1023/A:1010933404324>.
- [70] Friedman J, Hastie T, Tibshirani R. The elements of statistical learning. Springer Series in Statistics. NY, New York: Springer; 2009.
- [71] Xu M, Watanachaturaporn P, Pramod KV, Manoj KA. Decision tree regression for soft classification of remote sensing data. Remote Sens Environ 2005;97(3): 322–36. <https://doi.org/10.1016/j.rse.2005.05.008>.
- [72] Vapnik VN. English translation Estimation of dependencies based on empirical data. New York, NY: Springer-Verlag; 1982.
- [73] Vapnik VN. Statistical Learning Theory. NY, New York: John Wiley & Sons; 1998.
- [74] Rodriguez-Pérez R, Bajorath J. Evolution of support vector machine and regression modeling in chemoinformatics and drug discovery. J Comput -Aided Mol Des 2022; 36:355–62. <https://doi.org/10.1007/s10822-022-00442-9>.
- [75] Balfer J, Bajorath J. Systematic artifacts in support vector regression-based compound potency prediction revealed by statistical and activity landscape analysis. PLoS One 2015;10(3). <https://doi.org/10.1371/journal.pone.0119301>.
- [76] ICITECH – Instituto Universitario de Ciencia y Tecnología del Hormigón – UPV (<https://icitech.webs.upv.es/index.php/en/presentation/>).
- [77] Computer and Structures I. SAP2000. Advanced 25. Structural Analysis Program-Manual. Berkeley, California, USA: Computer and Structures, Inc; 2025.
- [78] Python Software Foundation. Open-Source Programming Language. Python: A Dynamic. Python Software Foundation; 2015 (<https://www.python.org/pf/>).
- [79] Parisi F, Mangini AM, Fanti MP, Adam JM. Automated location of steel truss bridge damage using machine learning and raw strain sensor data. Autom Constr 2022; 138(1). <https://doi.org/10.1016/j.autcon.2022.104249>.
- [80] Parisi F, Ruggieri S, Lovreglio R, Fanti MP, Uva G. On the use of mechanics-informed models to structural engineering systems: application of graph neural networks for structural analysis. Structures 2023;59. <https://doi.org/10.1016/j.struc.2023.105712>.
- [81] Mangalathu S, Hwang S-H, Choi E, Jeon J-S. Rapid seismic damage evaluation of bridge portfolios using machine learning techniques. Eng Struct 2019;201. <https://doi.org/10.1016/j.engstruct.2019.109785>.
- [82] Agarwal P, Priyaranjan P, Mehta PK. Box-girder bridges - modelling and analysis. Int J Eng Model 2022;35(1):19–42. <https://doi.org/10.31534/engmod.2022.1.ri.02m>.